

Homogeneous Ice Nucleation in Subtropical and Tropical Convection and Its Influence on Cirrus Anvil Microphysics

ANDREW J. HEYMSFIELD, LARRY M. MILOSHEVICH, CARL SCHMITT, AND AARON BANSEMER

National Center for Atmospheric Research, Boulder, Colorado*

CYNTHIA TWOHY

College of Oceanic and Atmospheric Sciences, Oregon State University, Corvallis, Oregon

MICHAEL R. POELLOT

Department of Atmospheric Sciences, University of North Dakota, Grand Forks, North Dakota

ANN FRIDLIND

NASA Ames Research Center, Moffett Field, California

HERMANN GERBER

Gerber Scientific Inc., Reston, Virginia

(Manuscript received 23 March 2004, in final form 12 July 2004)

ABSTRACT

This study uses a unique set of microphysical measurements obtained in a vigorous, convective updraft core at temperatures between -33° and -36°C , together with a microphysical model, to investigate the role of homogeneous ice nucleation in deep tropical convection and how it influences the microphysical properties of the associated cirrus anvils. The core and anvil formed along a sea-breeze front during the Cirrus Regional Study of Tropical Anvils and Cirrus Layers–Florida Area Cirrus Experiment (CRYSTAL–FACE).

The updraft core contained two distinct regions as traversed horizontally: the upwind portion of the core contained droplets of diameter $10\text{--}20\text{ }\mu\text{m}$ in concentrations of around 100 cm^{-3} with updraft speeds of $5\text{--}10\text{ m s}^{-1}$; the downwind portion of the core was glaciated with high concentrations of small ice particles and stronger updrafts of $10\text{--}20\text{ m s}^{-1}$. Throughout the core, rimed particles up to 0.6-cm diameter were observed. The anvil contained high concentrations of both small particles and large aggregates.

Thermodynamic analysis suggests that the air sampled in the updraft core was mixed with air from higher altitudes that descended along the upwind edge of the cloud in an evaporatively driven downdraft, introducing free-tropospheric cloud condensation nuclei into the updraft below the aircraft sampling height. Farther downwind in the glaciated portion of the core, the entrained air contained high concentrations of ice particles that inhibit droplet formation and homogeneous nucleation.

Calculations of droplet and ice particle growth and homogeneous ice nucleation are used to investigate the influence of large ice particles lofted in updrafts from lower levels in this and previously studied tropical ice clouds on the homogeneous nucleation process. The preexisting large ice particles act to suppress homogeneous nucleation through competition via diffusional and accretional growth, mainly when the updrafts are $< 5\text{ m s}^{-1}$. In deep convective updrafts $> 5\text{--}10\text{ m s}^{-1}$, the anvil is the depository for the small, radiatively important ice particles (homogeneously nucleated) and the large ice particles from below (heterogeneously or secondarily produced, or recycled).

1. Introduction

The poorly understood processes of ice initiation in clouds can lead to large uncertainties in modeled precipitation, with implications for climate change studies. The ice formation process influences important cloud

characteristics, including precipitation rate and amount, dynamics, radiative properties, aqueous chemical processes, interstitial aerosols, electrification, vapor and liquid water concentrations, and appearance.

This study investigates the role of homogeneous ice

* The National Center for Atmospheric Research is sponsored by the National Science Foundation.

Corresponding author address: Andrew Heymsfield, NCAR, P.O. Box 3000, Boulder, CO 80307.
E-mail: heyms1@ncar.ucar.edu

nucleation in strong convection and its influence on the convectively generated cirrus microphysical composition of anvils. Cirrus ice particles can form on deliquesced aerosols without the need for ice nuclei, through homogeneous (spontaneous) ice nucleation. At temperatures between -35°C and -40°C , cloud droplets of diameter several microns or larger will freeze spontaneously, and at lower temperatures solution droplets smaller than $1\text{ }\mu\text{m}$ in diameter will freeze spontaneously (Heymsfield 1973, chapter 5; Sassen and Dodd 1988; Heymsfield and Sabin 1989; Rosenfeld and Woodley 2000). Ice particles, produced through heterogeneous ice nucleation or secondary processes at temperatures higher than about -35°C , can be lofted in deep convection to the temperatures where homogeneous nucleation occurs. Frozen cloud droplets deposited on the surfaces of ice particles provide a characteristic signature of lofting from lower storm levels, with a high likelihood of production via a nonhomogeneous ice nucleation mechanism.

Cirrus ice formation processes are strongly influenced by several factors:

- *Temperature:* Ice particles nucleated at temperatures above about -35°C are formed through some heterogeneous (nonhomogeneous) or secondary processes. Homogeneous nucleation becomes important when $T < -35^{\circ}\text{C}$ (Sassen and Dodd 1988; Heymsfield and Sabin 1989; Rosenfeld and Woodley 2000). Droplet concentrations measured in strong updrafts typically exceed 100 cm^{-3} and produce comparable concentrations of small homogeneously nucleated ice particles, whereas concentrations of heterogeneously nucleated ice particles are generally much lower.
- *Vertical air velocity:* The local cooling rate due to parcel lifting affects the ice supersaturation, droplet growth rates, and the concentration of ice crystals produced homogeneously.
- *Preexisting ice particles:* Ice particles produced in an updraft or entering through entrainment or sedimentation below the -35°C level deplete the water vapor and droplets and can potentially retard or suppress the homogeneous freezing process.

This study examines the homogeneous nucleation process in an environment of vigorous convection with preexisting ice particles, a research area not yet investigated. The primary observations in this study are from an aircraft penetration of a vigorous convective cell at a temperature near -35°C during the Cirrus Regional Study of Tropical Anvils and Cirrus Layers–Florida Area Cirrus Experiment (CRYSTAL–FACE) project in southern Florida. Microphysical data from convective core penetrations during several other field experiments are also presented. The instrumentation is described in section 2, and the primary aircraft measurements are presented in section 3. Sections 4–6 use thermodynamic and microphysical models to aid in interpreting the observations and in assessing the condi-

tions when the homogeneous ice nucleation process operates in updrafts with preexisting large ice particles.

2. Instruments and data analysis methods

Measurements used in this study were obtained by the University of North Dakota Citation aircraft in July 2002 during the CRYSTAL–FACE project in southern Florida. The focus of this study is an aircraft penetration of a convective core and associated anvil on 18 July 2002 from 1746 to 1750 UTC at a mean altitude of 9.98 km.

Temperatures were measured by two deiced Rosemount probes. In-flight evaluations lead to estimates of the absolute accuracy of the primary probe of $\pm 0.2^{\circ}\text{C}$ and the secondary probe measured $0.35^{\circ} \pm 0.07^{\circ}\text{C}$ lower than the primary probe during the cloud penetration. In convection and anvils, the Rosemount probes may overestimate the temperature due to blockage of the inlet by accumulating ice particles, (Lawson et al. 1998) or frozen cloud droplets (Heymsfield et al. 1979). Possible temperature errors from these effects are evaluated in section 3.

Water vapor mixing ratio was measured by a tunable diode laser (TDL) hygrometer (May 1998), then converted to relative humidity (RH) with respect to water using the temperature measurement. The accuracy of the RH measurement is a few percent RH as judged by Citation RH measurements when the RH is presumably close to water saturation, that is, supercooled liquid water (LW), low vertical velocity (w), and low ice water content (IWC), and close to ice saturation—no LW, no discernible updraft, and high IWC. Temperature errors impacting the RH measurements are discussed in section 3. The 3D winds, including the vertical air velocity (w), were derived using the approach outlined by Khelif et al. (1999) from the corrected aircraft ground speed and position and from five pressure ports on the radome gust probe that measure the aircraft's airflow attack and sideslip angles. In the straight flight and low liquid water contents during this penetration, the vertical winds are probably accurate to better than a few meters per second.

The presence of LW in particle sizes below about $50\text{-}\mu\text{m}$ diameter was detected by a Rosemount icing detector (RICE), and the liquid water content (LWC) was measured by a King probe. The RICE measurement provides an output voltage (V). This voltage can be calibrated for LWC measurement using the method of Mazin et al. (2001). This LWC detection threshold obtained by this method is very low, about 0.01 g m^{-3} at the Citation's airspeed. The use of the RICE also obviates the need to identify ice and water in small particles as would be required for imaging probes.

We used the following data to calibrate the RICE probe. The rate of ice sublimation in clear air following passage through a LW region is used to deduce a coefficient, k , that relates the rate of change of the RICE voltage, dV/dt , to the rate of accretion of liquid water,

from which the LWC is derived. Figure 1 shows the RICE voltage during the aircraft penetration, indicating no LW accretion in the anvil and glaciated portion of the updraft core ($t = 0$ –150 s), followed by accretion of LW where $dV/dt > 0$, followed by clear air where $dV/dt < 0$ due to sublimation of accreted frozen droplets. The constant k was derived from measurements in the sublimation region (Fig. 1b), using the mean value \bar{k} for the indicated time period when k was relatively constant. Figure 1c shows the corresponding LWC derived from k and dV/dt (solid), compared to LWC measured by the King probe. King probe indication of LWC prior to $t = 150$ s is an artifact caused by sensing ice particles. According to the theoretical analysis given in Mazin et al. (2001), this method should yield an absolute accuracy in the 20%–30% range.

The particle size distribution (PSD) was measured by a PMS 2D-C probe and a SPEC Inc. high volume particle spectrometer (HVPS) imaging probe. The probes

span the size range from about $60\text{ }\mu\text{m}$ to 6 cm , with a sample rate of about 0.007 (2D-C) and $1\text{ m}^3\text{ s}^{-1}$ (HVPS). The techniques used to produce size distribution from the image data are described in Heymsfield et al. (2002). To ensure reasonable size distributions in each of 33 (unequal) diameter bins requires using 5-s averages, corresponding to approximately 600 m in the horizontal. The IWC was calculated from each 5-s PSD using the density–diameter relations for this cloud penetration given by Heymsfield et al. (2004).

Size distributions of droplets and small ice particles between $3.5\text{-}\mu\text{m}$ and $58\text{-}\mu\text{m}$ diameter, smaller than the size range of the 2D-C probe, were measured by a PMS forward-scattering spectrometer probe (FSSP). Particle sizes measured by the FSSP may be inaccurate if the particles are not spherical. FSSP concentrations may also be overestimated by a factor of 2 or more, if large ice particles are present, because they may break up on the inlet of the probe (Field et al. 2003). Nonetheless,

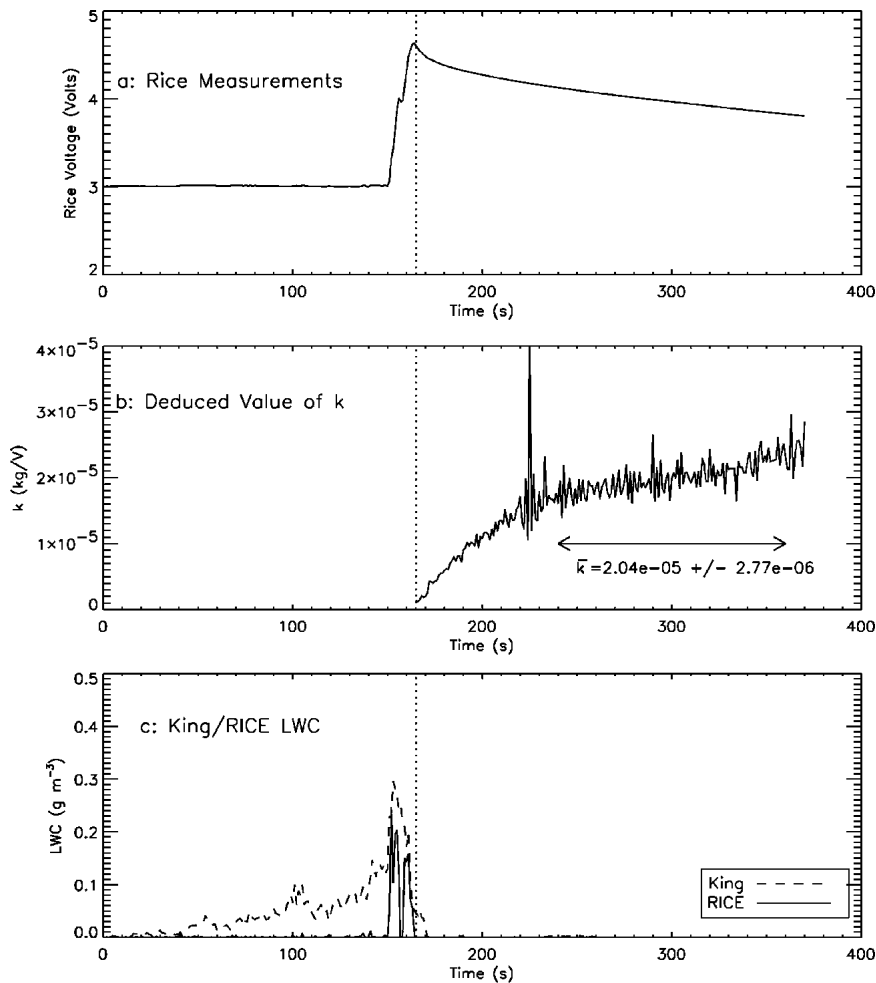


FIG. 1. Liquid water measurements during the aircraft penetration through the anvil ($t = 0$ –150 s), updraft core (150–165 s), then clear air. (a) RICE voltage, (b) deduced mean RICE calibration constant \bar{k} , and (c) derived LWC from the RICE probe (solid) and LWC measured by the King probe (dashed).

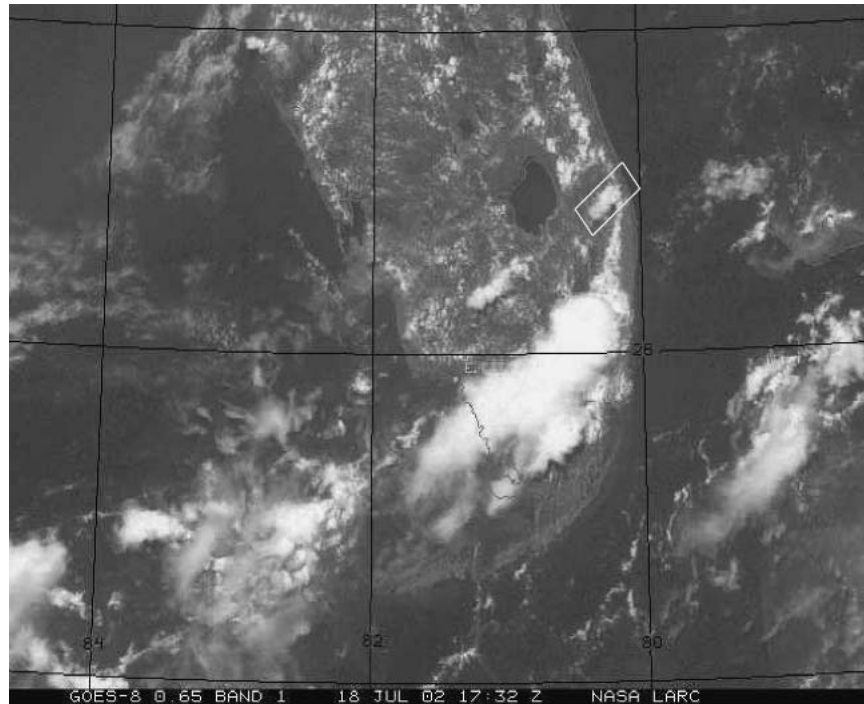


FIG. 2. *GOES-8* satellite image of the penetrated cloud (rectangular box), taken at 1732 UTC, about 14 min prior to the aircraft penetration.

the RICE LWC measurements place constraints on the FSSP droplet concentrations and diameters.

High-resolution particle images were obtained from the SPEC Inc. Cloud Particle Imager (CPI), with a nominal resolution of about $2\ \mu\text{m}$ and a minimum detectable size of about $20\ \mu\text{m}$. In the critical size range $20\text{--}150\ \mu\text{m}$, the CPI data could not be used to construct PSDs because there were too few particles in the 5-s averaging intervals. The CPI data are mainly used to provide detailed information on ice particle habits above about $30\text{-}\mu\text{m}$ diameter.

The condensed water content (CWC), equal to the sum of the LWC and IWC for particles larger than about $6\ \mu\text{m}$ in diameter, was measured using a counterflow virtual impactor (CVI; Ogren et al. 1985; Twohy et al. 1997), with an absolute accuracy of about 20%. Extinction in visible wavelengths was measured directly for sizes above about $5\text{-}\mu\text{m}$ diameter using a cloud integrating nephelometer (CIN) probe (Gerber et al. 2000).

3. Aircraft observations

The convective cloud focused on in this study formed over land along the east coast of Florida in association with a sea-breeze front (Fig. 2). The cloud first appeared in the *Geostationary Operational Environmental Satellite-8* (*GOES-8*) visible satellite imagery at 1615 UTC, located near 26.9185°N , 80.1787°W . By 1732 UTC the cloud developed an anvil that streamed southwest, downwind from the convective core. The GOES IR imagery indicated that the cloud had reached the

tropopause near 14-km altitude by the time of the aircraft penetration at 1746 UTC.

The Citation penetrated the cloud from west to east (downwind to upwind), as indicated by the numbered positions in Fig. 3. Wind vectors plotted along the aircraft track in Fig. 3 indicate that the wind direction in the anvil was primarily northeasterly, reflecting the storm-relative environmental midlevel flow, and weak easterly in the updraft core, presumably reflecting the predominant low-level origin of the updraft air.

The cloud penetration is separated into four distinct regions, as shown in Fig. 3, based on the aircraft measurements of w and RH (Figs. 4a and 4b). Proceeding upwind, the aircraft first encountered the anvil (labeled A, Fig. 3), which is characterized by relatively weak vertical velocities and RH near ice saturation. Characteristics of the updraft core change markedly in the center of the core. In the downwind portion of the core (B), the vertical velocity is up to $20\ \text{m s}^{-1}$ and is 5%–10% RH supersaturated with respect to ice.¹ The up-

¹ An error in the temperature measurements due to blockage of the inlet blockage by icing or ingested ice particles would yield errors in RH. Either case produces temperatures that are too low (Heymsfield et al. 1979). Assuming that the TDL water vapor density of about $0.39\ \text{g m}^{-3}$ as measured in the updraft core (B) was correct, water saturation would imply an air temperature of -31.6°C . Because no LW was measured by the very sensitive RICE probe, the RH must have been at or below water saturation, implying that the updraft core temperatures were between -31.6° and -33°C .

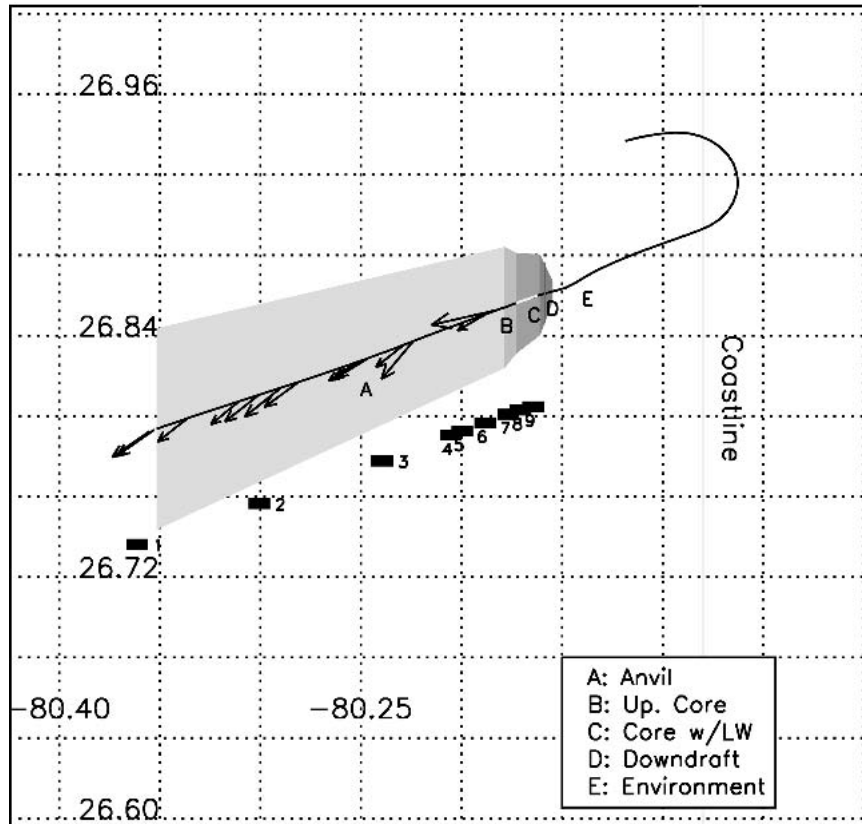


FIG. 3. Sketch showing the flight track of the Citation through the updraft core. The flight direction was into the wind, (left to right). The vectors show the measured horizontal winds, with vector length indicating the relative speed and arrow the direction. The five primary cloud region are identified as A to E, and different shading identifies the area comprising each region. Numbered squares, 1 to 9, indicate points along the aircraft track where particle size distribution and habit data are examined (shifted below the track for clarity).

wind portion of the core (C) contains LW and is highly supersaturated with respect to water, despite the lower peak vertical velocity of 10 m s^{-1} , indicating that vapor depletion from ice growth in the stronger updrafts far exceeds the depletion in the LW region. The extreme water supersaturation in the LW region will be shown from calculations in section 5 to be entirely reasonable. The temperature in the LW region, -35.3°C , is at or near the threshold for homogeneous nucleation, and these droplets are either in the process of freezing homogeneously or will soon do so.

Immediately upwind from the updraft core is a strong downdraft (D), containing ice particles; these particles were presumably carried downward to the aircraft level. Severe turbulence was encountered at the boundary of regions C and D. The equivalent potential temperature (θ_e , Fig. 4d) decreased through the LW region (C) and is a minimum near the turbulent boundary. The upwind, out-of-cloud environment had low RH.

The microphysical measurements during the cloud penetration are summarized in Fig. 5. The peak CWC

measured by the CVI is about 1.1 g m^{-3} in the glaciated portion of the core (Fig. 5a, region B) and the CWC decreases with distance both downwind in the anvil and upwind in the LW region (C). The LWC derived from the RICE measurements, about 0.2 g m^{-3} ($\pm 20\%$ – 30% ; Mazin et al. 2001), is relatively small in comparison to CWC. The IWC as derived from the imaging probes for sizes $> 50 \mu\text{m}$ in the anvil (A) is about twice the IWC due to small particles ($5\text{--}56 \mu\text{m}$) calculated from the FSSP measurements. However, in the updraft core (both regions B and C) the contributions of small particles to the IWC exceeds the contribution of particles $> 50 \mu\text{m}$ measured by the imaging probes. The optical extinction (σ) peaks in regions B and C and in the updraft core is dominated by FSSP-size particles (Fig. 5c). These σ values were derived from twice the measured total cross-sectional area of the FSSP size distributions (assuming spherical particles) and also from the combined 2D/HVPS size distributions (taking the imaged areas of the particles). Direct measurements of σ from the CIN probe mirror the values derived from the FSSP and further verify that extinction

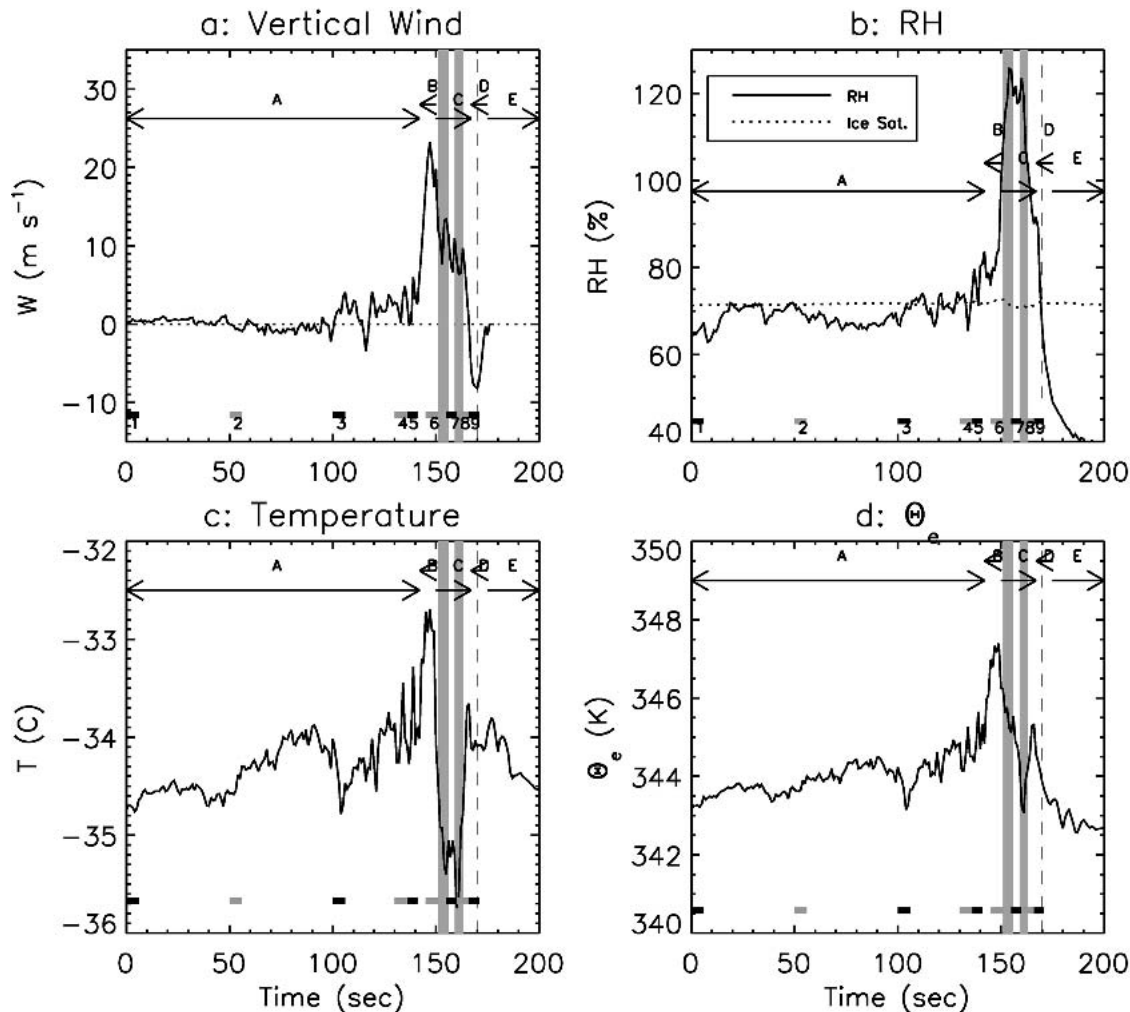


FIG. 4. Citation data from the cloud penetration: (a) vertical winds, (b) RH, (c) temperature, (d) equivalent potential temperature. LW regions are shown by vertical shading. Cloud regions are labeled as in Fig. 3.

in the updraft core is dominated by contributions from small particles and that the assumption of spherical particles is a good one. Figures 5e and 5f show that the small (FSSP) particles in the LW region (C) are more numerous (up to 200 cm^{-3}) and smaller ($17\text{-}\mu\text{m}$ mean diameter) than the small particles in the glaciated region (B) of the core (80 cm^{-3} , $26\text{-}\mu\text{m}$ mean diameter). Whether liquid or ice, the extinction and CWC of the core is dominated by small particles, unlike the anvil at this altitude.

Particle images from the CPI (Fig. 6) corresponding to the numbered locations in Figs. 3–5 show how the particle characteristics change across the penetration. Positions numbered 1–3 are in the anvil (region A), 4 and 5 are near the updraft core, 6 is in the glaciated portion of the core (B), 7–8 are in the LW portion of the core (C), and 9 is in the downdraft (D). Region C contains many droplets (liquid is indicated by the interference rings), with low concentrations of larger par-

ticles including graupel. More complex shapes, and aggregates, become more rounded and smaller near the downwind end of the anvil as the particles sublimate. Both small and large particles are found throughout the anvil. Note that the downdraft (D) contains both small particles and graupel, presumably carried down from above. Images from the 2D-C and HVPS probes were similar but with lower resolution.

The 1-Hz FSSP size distributions at each of the nine numbered positions along the flight track (Pos.) are shown in Fig. 7. Both the FSSP concentration (N_t), listed in each panel) and the LWC assuming that all FSSP particles are liquid (F) increase in the anvil toward the updraft core. In the LW region ([7] and [8]) the size distributions are dramatically different with very high concentrations in the second ($7\text{--}10 \mu\text{m}$) size bin and the RICE LWC (R) indicates that about 35%–40% is from droplets. Other FSSP size distributions in the LW region (not shown) were bimodal, with the

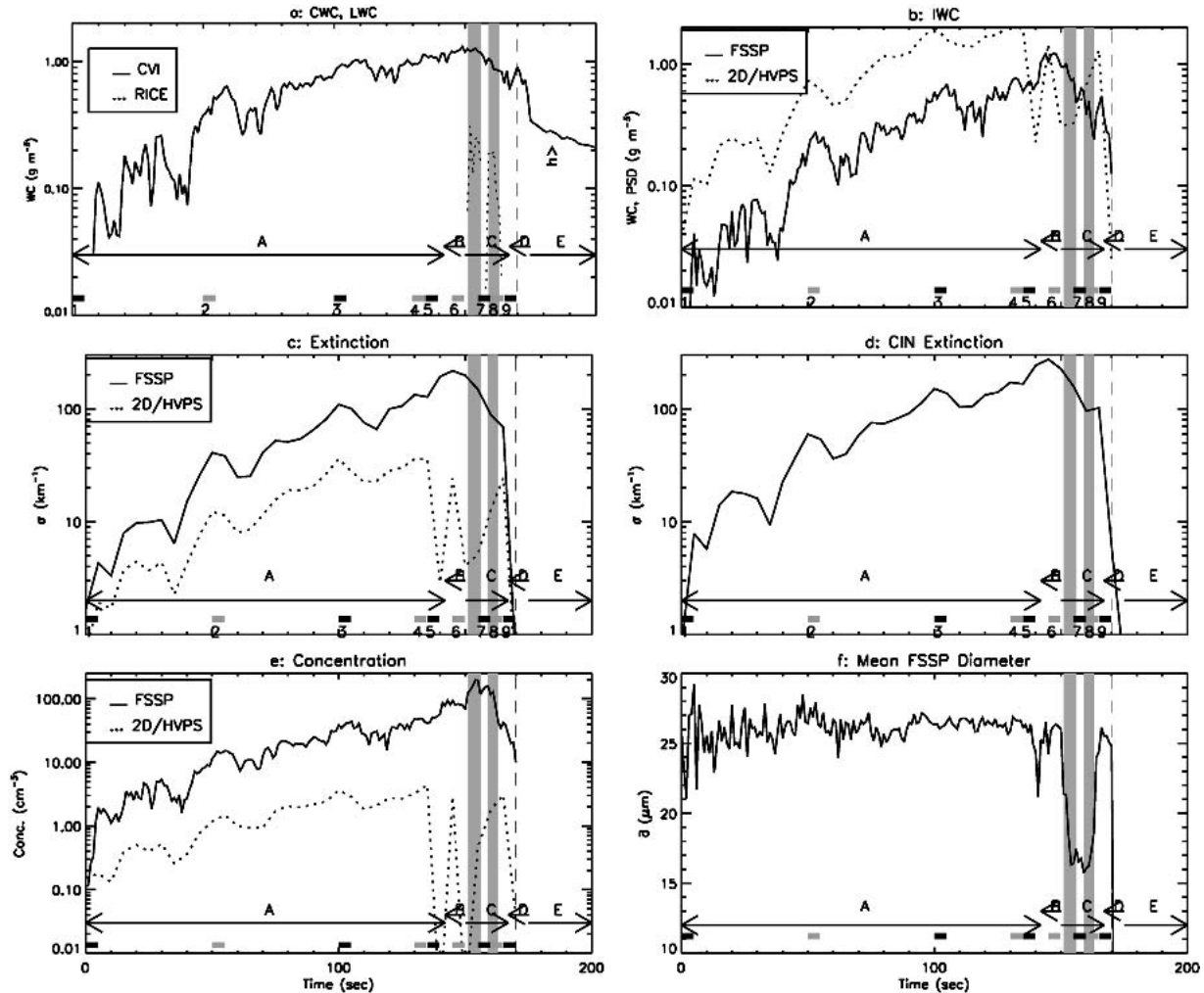


FIG. 5. Microphysical quantities measured during the cloud penetration. Vertical shading indicates LW was measured by the RICE. (a) CWC measured by the CVI and LWC measured by the RICE. The annotation “h” refers to residual water in the CVI inlet following passage through a cloud (hysteresis). (b) IWC in the size range 5–56 μm calculated from FSSP measurements assuming that the particles are solid ice spheres, and IWC above 50 μm from the imaging probe size distributions. (c) Extinction from the particle probes. (d) Extinction measured by the cloud integrating nephelometer. (e) Total concentration from the particle probes for their respective size ranges. (f) FSSP mean diameter. Numbered squares corresponds to size distributions plotted in later figures.

smallest (presumably droplet) mode in the size range 5–12 μm . The size distribution in the downdraft is similar in shape and concentration to those in the anvil. Note the lower concentration of particles smaller than about 15 μm in the ice region adjacent to the LW (first and last panels), consistent with the absence of LW measured by the RICE.

The probability of a given droplet freezing spontaneously increases with its volume, so the largest droplets tend to freeze first and the smallest last, such that at an intermediate stage of the homogeneous nucleation process the small end of the FSSP size distribution would be primarily liquid and the large end primarily ice (ignoring for now preexisting ice). Although there will be overlap of the droplet and ice modes in the size distributions the RICE LWC measurements can be used to

estimate the maximum liquid droplet sizes by integrating the FSSP size distribution from the small end until the measured LWC is reached. The cumulative distribution of LWC obtained by integrating the FSSP-measured 1-Hz size distributions from small to large sizes when the RICE detected LW is shown in Fig. 8. The LWC measured by the RICE is accounted for by the portion of the size distribution smaller than about 20–25 μm , and constituting about 30%–40% of the CWC in the FSSP range, but dominating the total concentration. Some larger droplets may still be present (Fig. 6), but in low concentrations and comprising low LWC.

Size distributions from the imaging probes for particles larger than 50 μm are shown in Fig. 9 at the nine positions indicated in Figs. 3–5. The distributions for

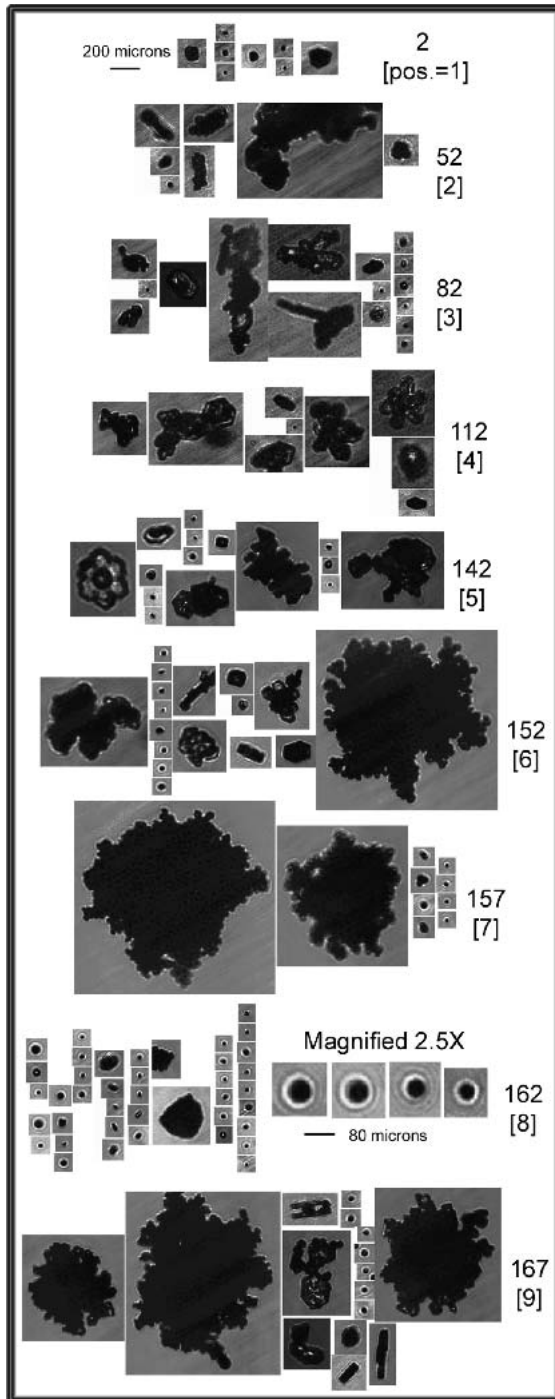


FIG. 6. Representative CPI images corresponding approximately to the numbered locations in Figs. 3–5. Positions numbered 1–3 are in the anvil (region A), 4 and 5 are near the updraft core, 6 is in the glaciated portion of the core (B), 7–8 are in the LW portion of the core (C), and 9 is in the downdraft (D).

two times (140–145 s and 150–155 s) are not shown because of artifacts in the 2D images (within regions of high electrical fields, as ascertained from Citation convective cloud measurements in earlier field programs)

that were not seen at other times. The maximum particle size is about 0.6 cm throughout much of the updraft, but is only about 0.3 cm in the downdraft portion of the anvil (positions 1 and 2) and at the upwind cloud edge (position 9). The first size bin (30–40 μm) dominates the concentration throughout the cloud, but the concentration in this size bin is lower in the LW region than in all regions except at the downwind edge of the anvil (positions 1 and 2), probably indicating that the 2D-C can measure the larger “ice mode” of FSSP sizes but not the smaller droplet mode. A composite FSSP and imaging probe size distribution for one 5-s period in the LW region (Fig. 10) shows that the probes agree well in the overlapping portion of their size ranges. The shaded portion of the FSSP size distribution, assumed to be predominantly droplets, is based on the analysis from Fig. 8 that the RICE LWC corresponds to the small end of the size distribution. Note that, although the small end of the PSD is liquid, there is a long tail that includes large rimed particles and graupel that are rising with the droplets in the updraft after presumably nucleating heterogeneously or by secondary processes at lower levels. The impact of preexisting ice on the homogeneous nucleation process will be investigated in section 6.

4. Entrainment–microphysics connection

Updraft thermodynamics, including the lapse rate, thermal buoyancy relative to the environment, extent of entrainment, and origin of the entrained air, may have a significant impact on the microphysical processes in the updraft core. The modeling and observations reported in Fridlind et al. (2004) suggest that ice crystals in the anvil for this and other CRYSTAL-FACE cases formed on midtropospheric aerosols rather than aerosols originating in the boundary layer, indicating that entrainment may play a significant role in the thermodynamics and microphysical properties of Florida convective clouds. In addition, aerosols may also have been entrained into the updraft. In this section, we examine the extent of entrainment into the updraft, followed in sections 5 and 6 by investigation of ice particle initiation in the updrafts.

We first investigate entrainment by comparing the observations to calculations from a simple parcel model with liquid and ice latent heating, lateral entrainment, and no precipitation (Heymsfield et al. 1978). Based on the radiosonde sounding from Miami 1431 UTC on 18 July at (100 km south of the cloud and two hours before the aircraft penetration), the model is initialized with a cloud base height of 800 m, a temperature of 22°C, and pressure of 933 hPa. These conditions are consistent with measurements from a Navy Twin-Otter research aircraft flying near the location of the Citation cloud penetration at about 1830 UTC. The cloud base updraft width is taken to be 5 km for the entrainment repre-

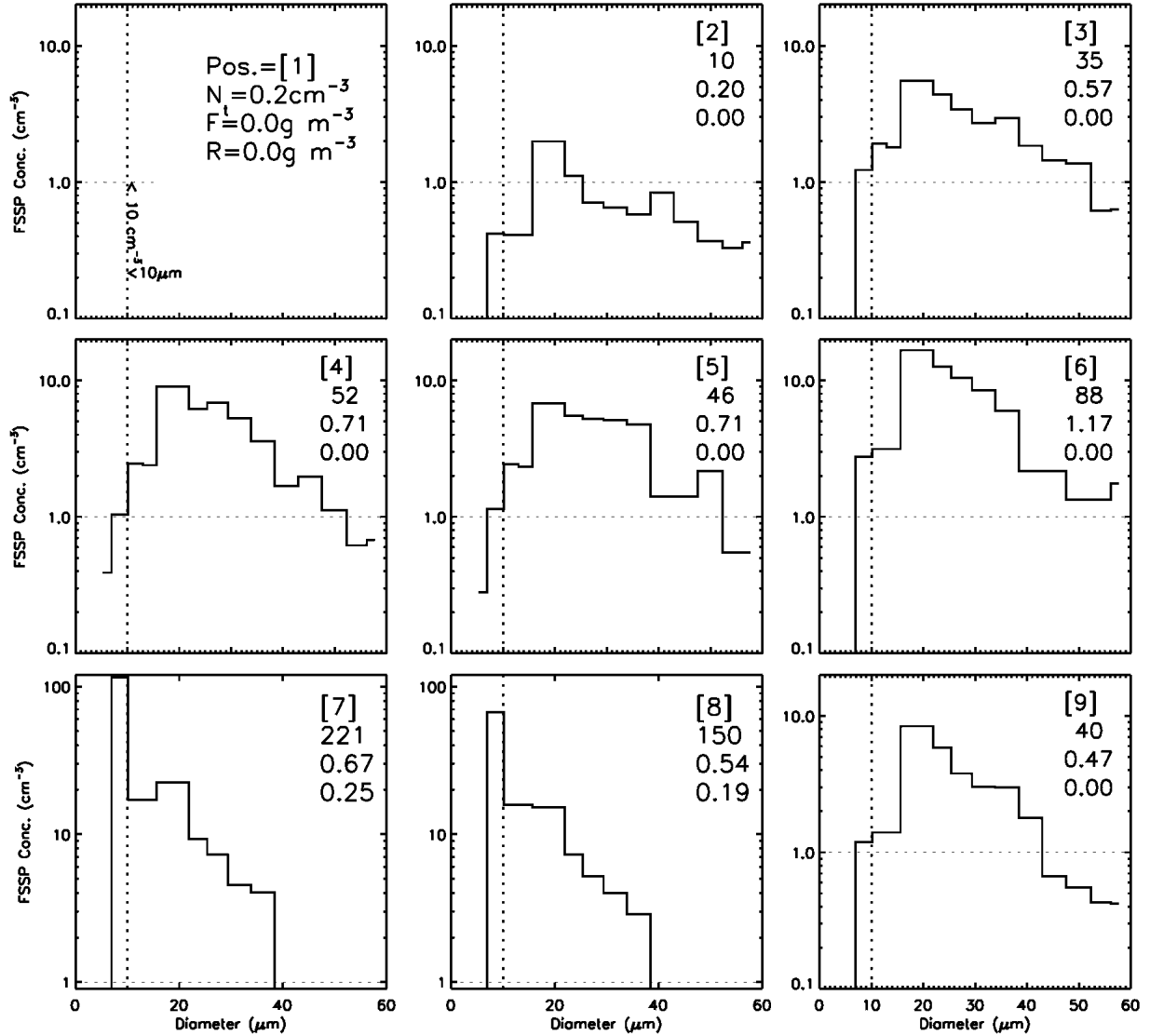


FIG. 7. FSSP 1-Hz size distributions at the nine labeled positions during the cloud penetration shown in Figs. 3–6. The numbers listed in each panel are position number (Pos.); total concentration (N , cm^{-3}); CWC for the FSSP size range, assuming the particles are liquid (F , g m^{-3}); and the LWC derived from the RICE (R , g m^{-3}). Dashed reference line indicates a concentration of 1 cm^{-3} .

sensation (see Hess 1959). This choice is not important because we investigate a range of fractional entrainment coefficients (fractional increase in air parcel mass per vertical kilometer of ascent) from 0.1 to 0.8. The calculations neglect fallout of precipitation, and effects of upper-level air transported downward (i.e., only lateral entrainment is considered).

If there is no entrainment or ice latent heating, the modeled temperature for adiabatic ascent is at least 7°C higher than the measurements (Fig. 11a, solid line); the modeled LWC is at least seven times larger than the CWC measured by the CVI (Fig. 11b); the modeled θ_e is about 10°C higher than measured in updraft (Fig. 11c); and the modeled vertical velocity, which includes condensate loading, is about twice the highest mea-

sured values (Fig. 11d). When latent heating due to homogeneous nucleation is forced in the model to occur linearly between -35° and -37°C (dotted curves that intersect the adiabatic curves at about -35°C), even larger differences from the observations are noted. Specifying a low entrainment coefficient of 0.1 leads to model results that are similar to the observations for T , w , and θ_e , but the modeled LWC is much greater than observed, probably because the observed LWC has been reduced by precipitation and by accretion on the large ice observed in the updraft. Although this model is simple, it is clear that entrainment is necessary to explain the observations.

A “Paluch diagram” (Fig. 12) can be used to investigate the altitudes at which the entrained air originated

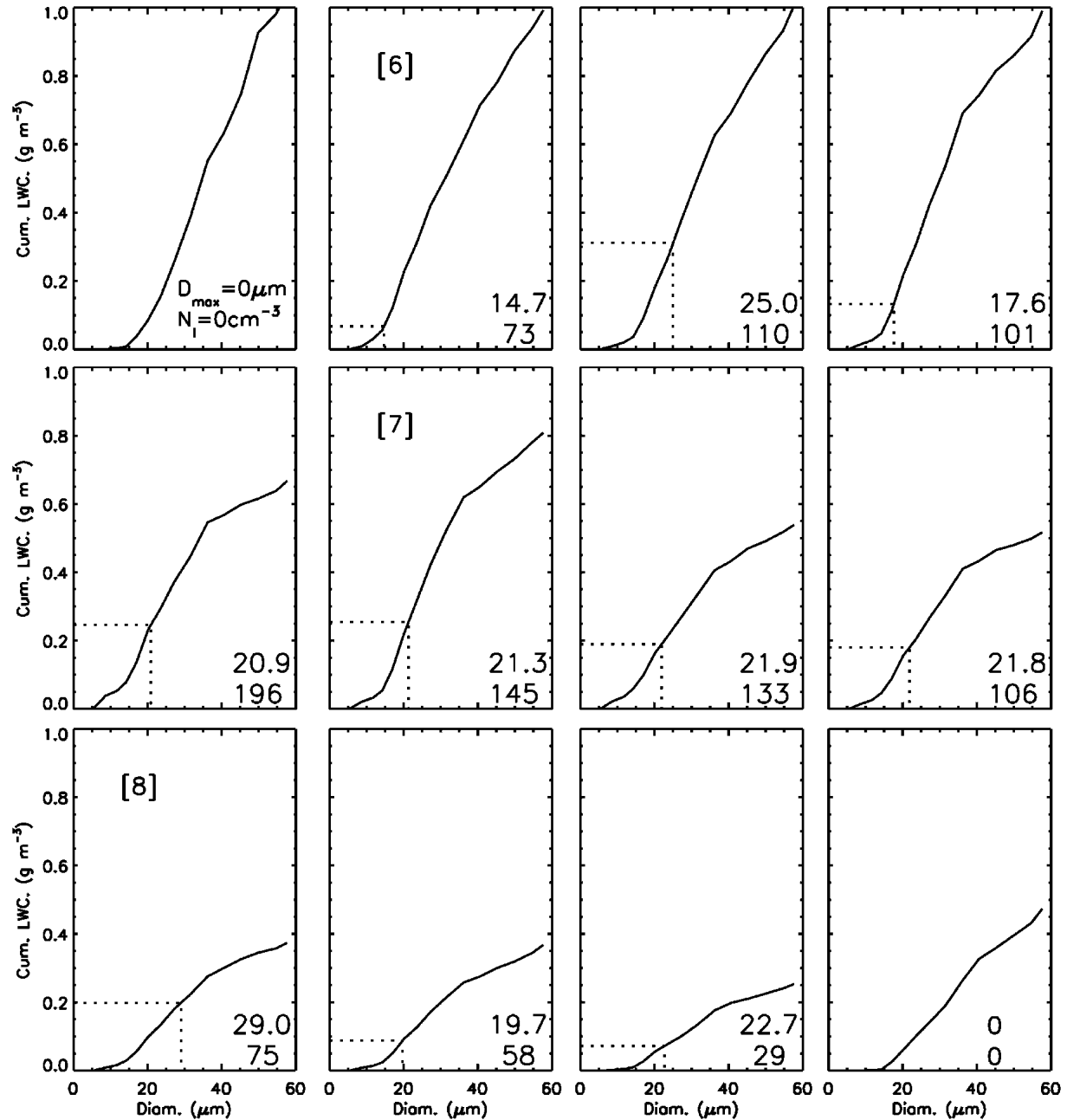


FIG. 8. Cumulative LWC distributions calculated from the 1-Hz FSSP size distributions for each second that LW was detected by the RICE probe, plus 1 s on either side. Horizontal lines show the LWC derived from the RICE data, and vertical lines show the corresponding maximum droplet diameter assuming that all smaller particles are droplets. This maximum diameter and the concentration of droplets are listed in each panel. Position numbers from Fig. 7 are shown in the appropriate panels.

and the extent of entrainment (Paluch 1979). Conceptually, the method draws upon two conserved properties that mix linearly in an updraft, the total water mixing ratio (Q) and the wet equivalent potential temperature (θ_q), here nearly equal to θ_e . The environmental Q and θ_q values in Fig. 12 were derived from the radiosonde sounding noted above, with labeled squares that indicate the altitudes. The cloud base height

(700–800 m) and associated Q and θ_q values were estimated from the sounding and from the Navy Twin-Otter measurements. The in-cloud Q and θ_q values calculated from the Citation measurements of CWC (from the CVI), humidity, temperature, and pressure are also shown in Fig. 12 (symbols), according to the region where the data were collected. Out of cloud (CWC, when $<0.01 \text{ g m}^{-3}$), environmental Q and θ_q values

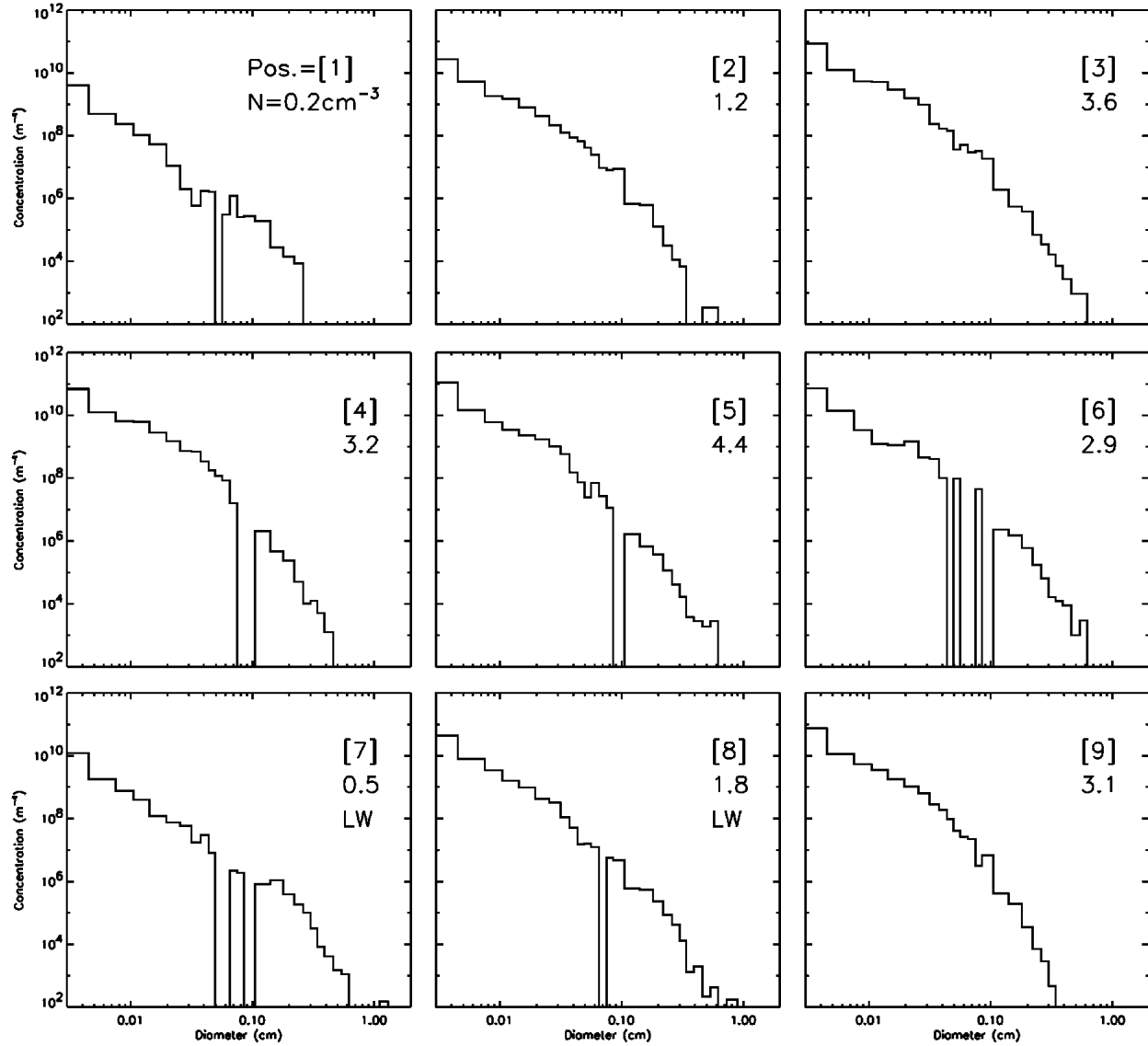


FIG. 9. Size distributions (5-s average) from the combined imaging probes at the nine locations defined in Fig. 3. The total concentration (cm^{-3}) for diameters above $30 \mu\text{m}$ are listed.

measured over the altitude range from 8.0 to 11.3 km in the vicinity of the cloud prior to and after the cloud penetration (6000 data points) fall on top of the sounding values (gray symbols in the figure) over the height range of interest here. Therefore, the sounding provides a good estimate of the actual out-of-cloud temperatures and the origin of the entrained air.

Using the concept outlined in Paluch (1979), a line labeled “mixing line” is fitted (by eye) through the in situ data points in Fig. 12 to show the origin of the mixed air. At the 10-km altitude of the Citation, there is a mixture of cloud base air and air that originated about 2 km above the aircraft level, near the upper part of the cloud (which was not sampled by the Citation).

There are a few caveats,² but they would have little effect on the interpretation of the heights at which the entrained air originated.

From the modeling and Paluch analysis, and the Citation measurements, we can infer that upper-level air

² The Paluch analysis does not include the effects of ice latent heating or precipitation fallout. The peak IWC of $1\text{--}2 \text{ g m}^{-3}$ observed in the updraft leads to a positive $1\text{--}2 \text{ K}$ increase in θ_q or θ_e . Therefore, θ_q would have been $1\text{--}2 \text{ K}$ lower than measured to be consistent with a Paluch-type analysis. The observed precipitation efficiency in the updraft would lead to a negative error in Q by as much as 50%. Despite these shifts (inset, Fig. 12), the analysis provides a powerful tool to study air parcel source regions.

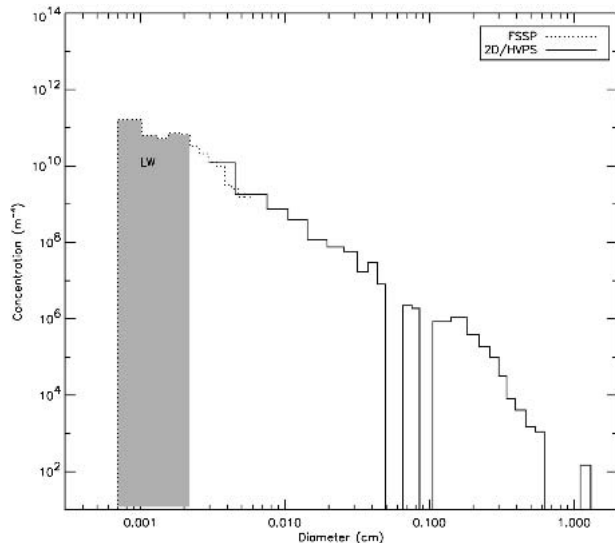


FIG. 10. Composite FSSP and imaging probe size distribution for a 5-s period in the LW region ($t = 152$ – 157 in Figs. 4–5). The highlighted portion of the FSSP size distribution is the size range presumed to be droplets from the analysis given in Fig. 8.

at the upwind cloud edge (C–D boundary) descended in a 7 m s^{-1} downdraft creating a shear zone (Fig. 4a, region D) where it mixed into the updraft core (region C), supplying CCN of midtropospheric origin into the updraft below the aircraft level, consistent with the midtropospheric origin of the aerosols reported by Fridlind et al. (2004). With lifting in the supersaturated updraft core, small cloud droplets could be produced, eventually freezing homogeneously near the Citation penetration altitude where the temperature has decreased to -35°C or below. Because the concentration of large ice particles in region D is very low (Fig. 5e), we infer that little ice was entrained into the LW region, presumably because the anvil particles on the upwind side of the cloud were carried around the core and downwind. In contrast, we hypothesize that the air entrained into the downwind glaciated portion of the updraft (region B) contained high concentrations of small ice particles nucleated homogeneously and mixed back into the updraft below the aircraft level, and this ice suppresses droplet growth and further homogeneous nucleation. We hypothesize that the microphysical and thermodynamic differences between the upwind and downwind portions of the updraft core (region B versus C) is largely attributable to the CCN entrained and whether or not it contains ice particles.

5. Homogeneous nucleation in the updraft

The glaciated portion of the updraft core with 20 m s^{-1} vertical velocities (B) contained no LW but high concentrations (80 cm^{-3}) of small ice particles ($<50 \mu\text{m}$). The adjacent LW portion of the updraft core with

weaker updrafts (C) contained high concentrations of cloud droplets (150 cm^{-3}). Both regions contained low concentrations of larger and often rimed ice particles that nucleated heterogeneously or by secondary processes at lower levels. We hypothesize that the high concentrations of small ice particles in region B were produced homogeneously and that the droplets in region C are in the process or will soon freeze homogeneously. In this section we use a 1D parcel model of droplet and ice crystal growth and homogeneous nucleation (Heymsfield and Miloshevich 1993) to assess whether the aircraft measurements are consistent with this homogeneous nucleation hypothesis and to gain insight into its importance in convectively generated cirrus.

The model is initialized with a CCN distribution of the form $N = cS^k$, where N is the concentration of CCN at water supersaturation S , and the coefficients $c = 150 \text{ cm}^{-3}$ and $k = 0.3$ yields droplet concentrations comparable to those observed in the LW region. The CCN composition is assumed to be ammonium sulfate, but this choice has little bearing on the results here because the droplets in the updrafts will be relatively large and dilute before they freeze. If entrainment occurs at temperatures below -35°C , CCN composition may be important. Homogeneous nucleation rates (J_H) are given by the chemical activity formulation of Koop et al. (2000), which treats the freezing of solution droplets in terms of the water activity; our model, with this formulation, allows for the freezing of solution droplets (haze particles) or activated cloud droplets. The droplet freezing rates calculated for large (pure water) $60\text{-}\mu\text{m}$ drops are almost identical to the laboratory measured rates at temperatures between -35.8°C and -37.1°C by Krämer et al. (1999).

A sequence of model runs for different vertical velocities in the range from 5 – 20 m s^{-1} is shown in Fig. 13 for initial conditions of 75% RH, 300 hPa , and a temperature of either -20°C or -28°C . These conditions are chosen to match the mean droplet sizes and concentrations observed by the aircraft in the LW region and assume that the droplets observed in the updraft initiated on entrained aerosols as discussed in the previous section. The role of large drops that originated at cloud base and large ice that nucleated heterogeneously at lower levels are discussed in section 6. Had we initialized our model at temperatures below -35°C , droplets would not have been activated as the humidity approached water saturation because haze particles frozen homogeneously would have prevented water saturation to have been reached. However, because entrainment is a phenomena that occurs principally in the lower and midcloud levels of convective cells and not in the upper levels where temperatures are mostly below -35°C , it is more likely that droplets rather than haze particles will freeze homogeneously.

All model runs share the common characteristics that, as the parcel rises and cools, the RH increases to

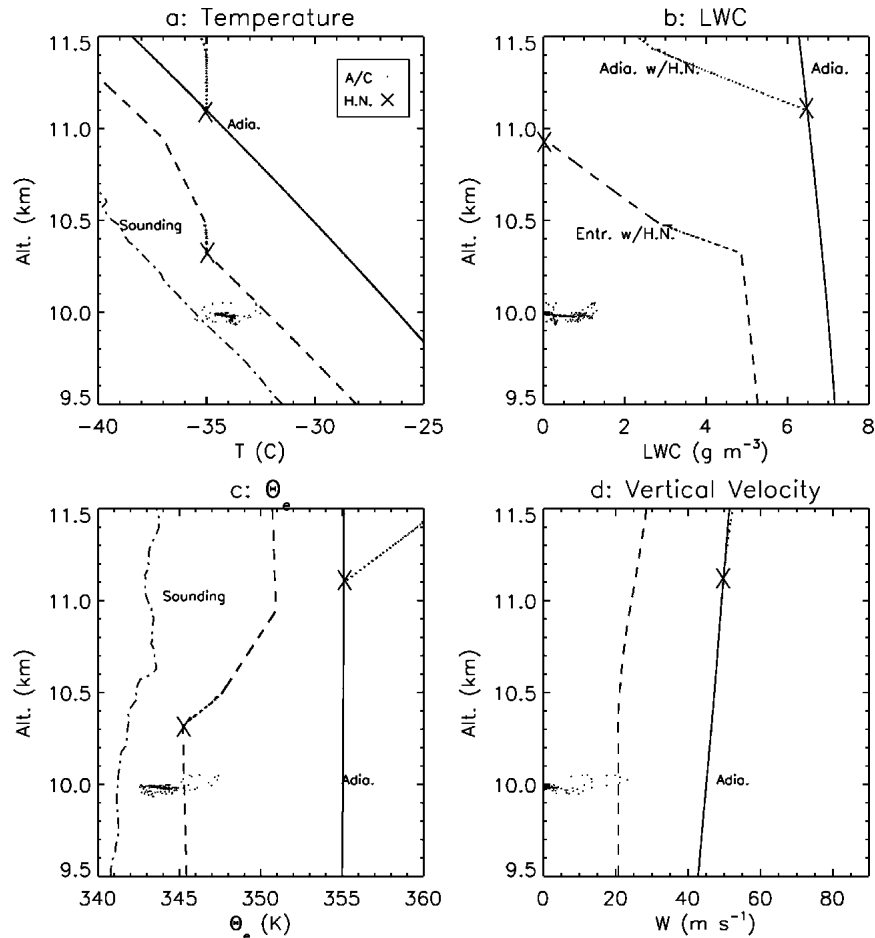


FIG. 11. Calculated profile of dynamic and thermodynamic properties using a simple 1D parcel model initialized at the observed cloud base conditions for the 18 Jul case. (a) Temperature. Solid line is moist adiabatic ascent that at “X” either continues as water or homogeneously freezes (dotted lines). Dashed line includes entrainment with homogeneous freezing beginning at X. Dash-dot curve is the sounding from Miami at 1435 UTC. Points are aircraft measurements during the cloud penetration. (b) LWC. (c) θ_e . (d) Vertical velocity (note the different altitude scale).

a maximum value of 105%–115% with respect to water depending on the updraft speed (Fig. 13a), then the RH decreases to near 100% RH as the vapor is depleted by the growth of activated droplets. Virtually all of the available CCN are activated in all the model runs, as was shown by the numbered points for these runs in Fig. 13c that indicate the peak droplet concentrations. Homogeneous nucleation occurs over the temperature range -35° to -37°C (Figs. 13c and 13d) where the ice concentration increases and the droplet concentration decreases. The runs initialized at -20°C (runs 1–3) produce larger droplets than the runs initialized at -28°C (18 versus $11\ \mu\text{m}$), which in turn produce large ice particles (22 versus $15\ \mu\text{m}$) and a greater IWC (0.5 versus $0.3\ \text{g m}^{-3}$, Fig. 13b).

As ice nucleation proceeds and the small ice particles grow rapidly in a highly ice-supersaturated environment, the RH quickly decreases to near ice saturation,

even in a $20\ \text{m s}^{-1}$ updraft (Fig. 13a), as is observed in region B. The model calculations are consistent with the dramatic difference in the RH observed between regions B and C and suggest that the small ice in the glaciated region could have been homogeneously nucleated. In the model, the concentration of homogeneously nucleated ice increases with increasing vertical velocity (Fig. 13c) because at lower vertical velocities the smaller droplets (which freeze last) evaporate before they freeze when the RH is reduced below water saturation by growth of the frozen larger droplets. This effect is seen in the odd shape of the mean ice diameter curves during ice nucleation (Fig. 13d) when smaller droplets freezing later in the process reduce the mean that previously was dominated by the larger droplets before they froze.

Above the homogeneous nucleation level in Fig. 13d, the ice particles grow little beyond their initial sizes

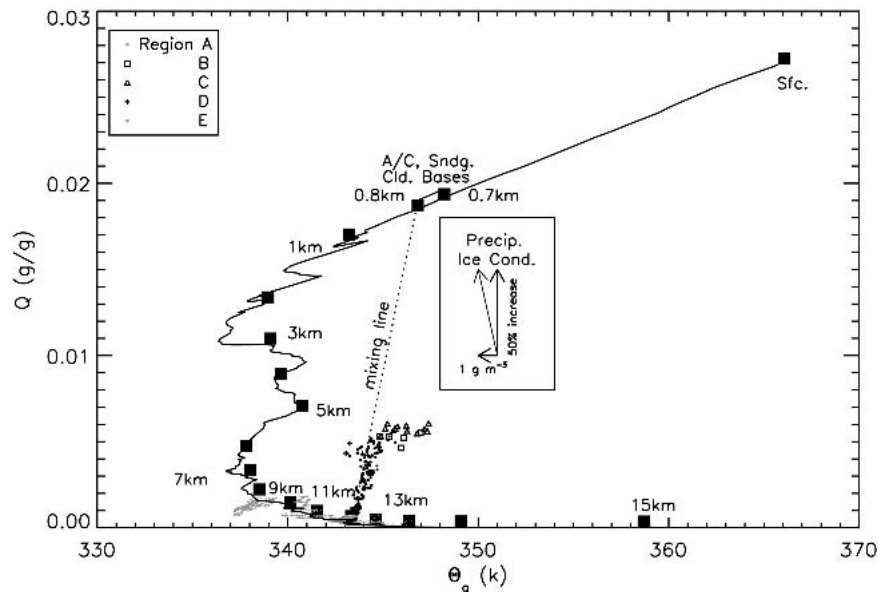


FIG. 12. Paluch diagram (total water mixing ratio vs wet equivalent potential temperature) for the 18 Jul convective cloud case. The sounding is from Miami at 1435 UTC, four hours before the aircraft penetration. See text for discussion of the cloud-base heights, mixing line, and vector showing contributions due to ice latent heating and precipitation fallout.

because there is little available water vapor. A hypothetical aircraft penetration at temperatures close to the homogeneous nucleation level would measure either 20–25- μm ice particles, or 10–20- μm droplets, or a mixture of both, consistent with the observations across the updraft core.

The mean droplet (or ice) diameter when homogeneous nucleation occurs depends on the amount of uplift after droplet activation (Fig. 13d, run 2 versus 4, numbered points), so the diameter of the observed droplets and small ice particles is related to the altitude at which CCN were introduced into the updraft. The temperature range over which homogeneous nucleation occurs and its dependence on the droplet diameter is investigated, in Fig. 14 for a 10 m s^{-1} updraft, by initializing model runs at successively higher temperatures and thereby allowing successively greater amounts of droplets growth before homogeneous nucleation begins. Each curve shows the fraction of droplets that are frozen as a function of temperature for a model run that is initialized at the indicated cloud base temperature (T_{cb} , below curve). The resulting mean droplet diameter just prior to the onset of homogeneous nucleation is shown above each curve. The freezing process for a given mean droplet size is completed within a 1°C temperature range ($< 100 \text{ m}$ of uplift) and begins at -34.5°C for 100- μm droplets and -38°C for 3- μm droplets. Figure 14 also shows that droplets of the mean diameter observed in region C (dashed curve) would begin to freeze in the temperature range -36° to -37°C , consistent with the observation of LW at -35.5°C . The observations are also

consistent with droplets that originated at about the -24°C level (but in reality would not be introduced in a single location).

The model results are consistent with the observation of LW in region C and the inference that homogeneous nucleation will soon occur, but the model results are not consistent with the observation in region B that high concentrations of small ice particles (80 cm^{-3}) but no LW are present at a temperature of -33°C . Figure 13a shows that LW cannot exist in the presence of high concentrations of small ice particles because the RH will be near ice saturation, even in a 20 m s^{-1} updraft. The high ice concentrations in region B must have either formed heterogeneously at lower levels and then suppressed droplet growth and homogeneous nucleation in this portion of the updraft core (but not in region C), or else the ice particles did nucleate homogeneously not far above the aircraft level (as presumably occurs in region C) and were subsequently transported downward and entrained back into the updraft, suppressing further homogeneous nucleation.

The analysis in the previous section indicated that some of the entrained air originated above the aircraft level and brought CCN into the updraft below the aircraft level, but the air entrained into the upwind side of the core (region C) did not contain ice because it is carried downwind. We suggest that the same homogeneous nucleation process was operative throughout the updraft core in the early life of the cloud, and the subsequent suppression of further homogeneous nucleation in only region B is ultimately attributable to the mean environmental airflow and its influence on the

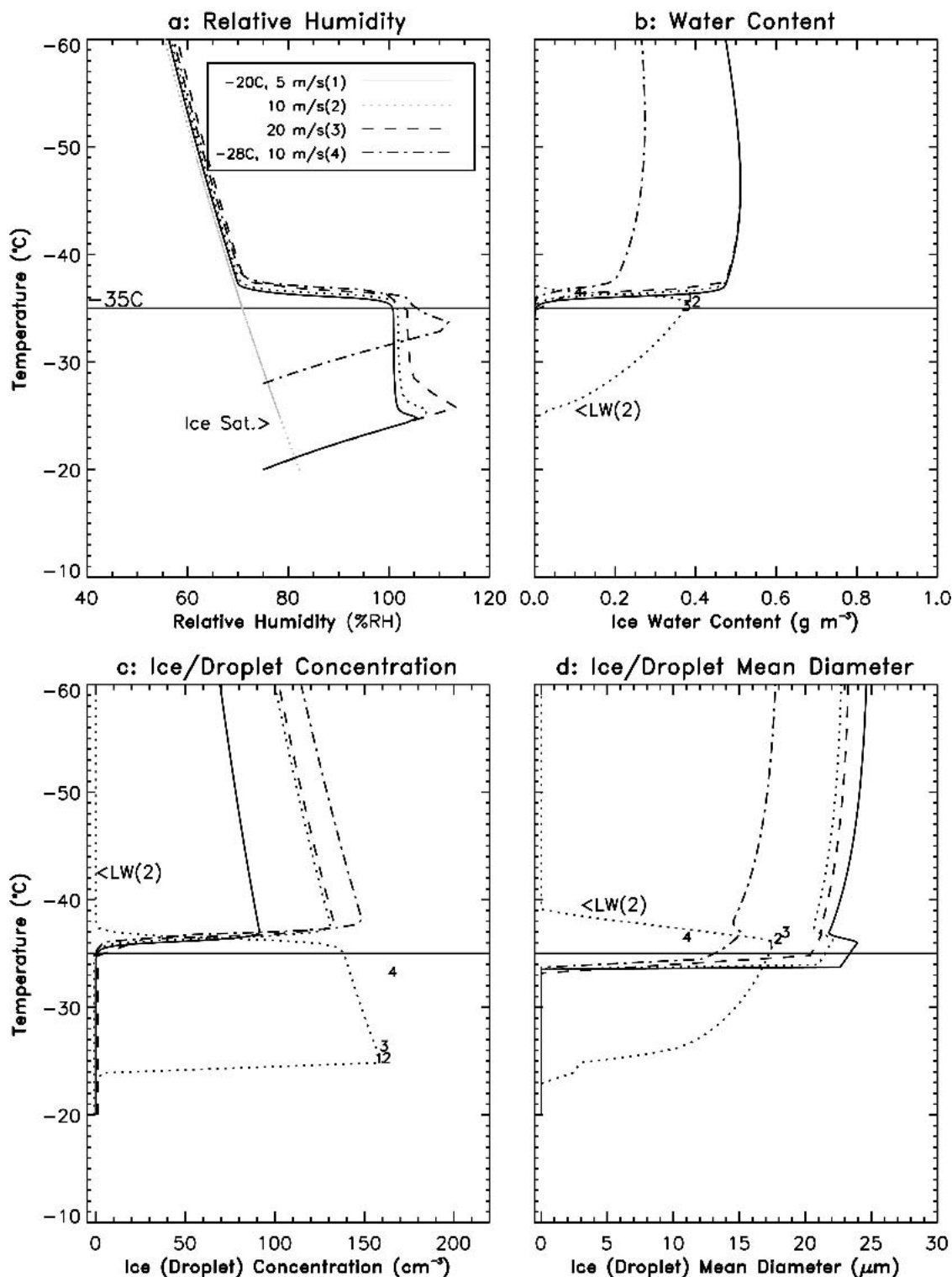


FIG. 13. Calculations of cloud properties from a 1D parcel model that simulates droplet and ice growth and homogeneous ice nucleation for four model runs with updraft velocities of 5, 10, and 20 m s⁻¹. The model was initialized at temperatures of either -20° or -28°C. The liquid phase calculations are shown for the 10 m s⁻¹ run [LW(2)]. (a) Relative humidity with respect to water, including the ice saturation curve. (b) IWC. (c) Ice concentration. (d) Ice mean diameter. Numbers in (c) and (d) show the values of the maximum values for the liquid phase, and the T where the maximum occurs. The curve labeled “LW(2)” for run 2 (which approximates the observed vertical velocity in the LW region) illustrates the simultaneous decrease in droplet concentration and mean diameter through the homogeneous nucleation zone.

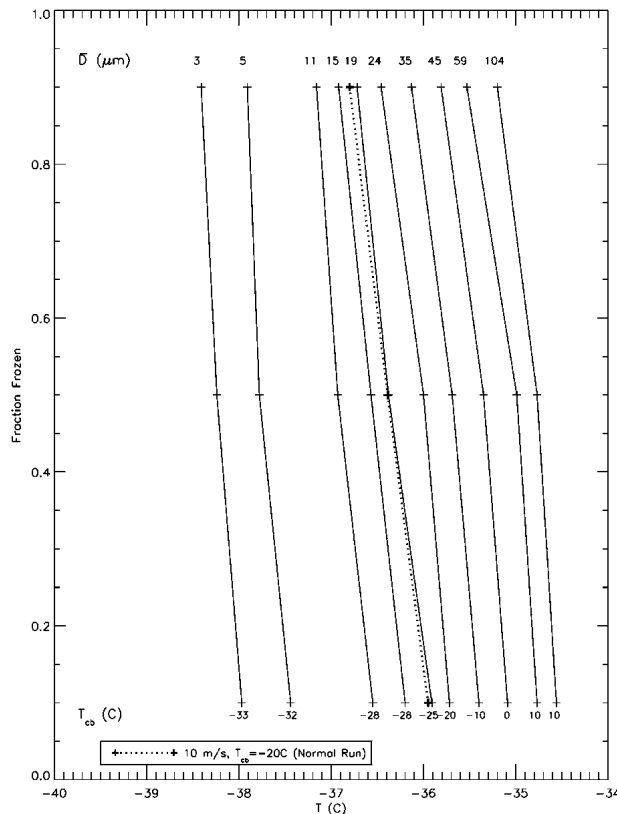


FIG. 14. Calculations of the fraction of a population of droplets frozen homogeneously as a function of temperature, for model runs initialized with a vertical velocity of 10 m s^{-1} at the cloud base temperatures (T_{cb}) shown. The population mean droplet diameter (\bar{D}) is shown above each curve. Duplicate T_{cb} values with different \bar{D} use different CCN spectra. A model run for run 2 from Fig. 11 is shown by the dotted curve.

presence of ice in air that is transported downward and mixed into the updraft core.

6. Influence of preexisting ice on homogeneous nucleation

The observations and entrainment interpretations depict an updraft that contains “preexisting” large ice particles ($> 100 \mu\text{m}$) together with small ice and recently activated droplets lofted in updrafts to near the homogeneous nucleation zone. The role of the large particles in reducing the numbers of homogeneously nucleated ice particles, through vapor and droplet depletion, was not considered in the homogeneous nucleation model in section 5 nor in previous studies. Both the observations in region B and the model calculations in Fig. 13a showed that vapor depletion from the growth of high concentrations of small ice particles is sufficient to reduce the RH to near ice saturation and suppress the homogeneous nucleation process, even in a 20 m s^{-1} updraft. However, the lower concentrations of large ice particles in the 10 m s^{-1} updrafts of region

C were evidently unable either to substantially accrete the small droplets nor reduce the vapor excess. The calculations presented in this section are used to assess whether CCN entrained into the updraft could be activated and grow as droplets from below, and to explore the effects of the preexisting ice on the homogeneous nucleation process in convection. Note that the results presented in this section should be taken only as a guide that illustrates the influence of preexisting ice on the homogeneous nucleation process because specific values will depend on the ice size distributions, the temperature level at which droplets form, and other factors.

a. Droplet activation on entrained CCN

We first consider whether the droplets observed in region C could have been activated on entrained CCN, given the preexisting ice particles that would have served to deplete the water vapor. Water vapor in the adiabatic model in section 5 is determined by the vertical velocity (w) and the growth rate of the droplet and homogeneously nucleated ice particles:

$$\frac{ds}{dt} = \phi_1 w - \phi_2 \frac{dX_l}{dt} - \phi_3 \frac{dX_i}{dt}, \quad (1)$$

where s is the (water) saturation ratio ($\text{RH}/100$), X_l and X_i are the liquid and ice mixing ratios, and ϕ_1 , ϕ_2 , and ϕ_3 are proportional to s and are dependent upon temperature and pressure (Heymsfield 1975; Heymsfield and Sabin 1989). In this adiabatic approach, the total water mixing ratio (vapor plus condensate) is a conserved quantity.

The homogeneous nucleation model has been modified to include an extra vapor depletion term:

$$\phi_3 \frac{dX_0}{dt}, \quad (2)$$

where X_0 is the mixing ratio of the preexisting ice. This mixing ratio is derived using a gamma-type size distribution, $N(D) = N_0 D^\mu e^{-\lambda D}$, represented in terms of a scale factor (N_0), the dispersion (μ), the slope (λ), and minimum and maximum cutoff diameters. Analysis of the aircraft size distribution data through the cloud penetration indicates the λ range from 6 to 66 cm^{-1} and μ range from -1.84 to -0.79 . The preexisting ice is taken to cover the size range $100 \mu\text{m}$ to 0.3 cm and to have bulk densities of 0.15 g m^{-3} (as derived for this penetration; Heymsfield et al. 2004). A given initial IWC (IWC_0), λ , and μ (varied according to λ , see the appendix), when taken in 33 bins over this size range and for the assumed ice bulk density, implies a given N_0 and a PSD.

The threshold conditions that will prevent droplet formation and hence homogeneous nucleation can be estimated analytically for the preexisting ice from Eq. (1). At precisely water saturation ($s = 1.0$) and with no droplets present ($dX_l/dt = 0$), droplets will only form if

the updraft can overcome vapor depletion by ice and increase the RH ($ds/dt > 0$). At the threshold $ds/dt = 0$, droplets can form if $\phi_1 w > \phi_3 dX_0/dt$. Each panel in Fig. 15 shows the updraft speed that just balances vapor

depletion by ice as a function of IWC, for five different spectral slopes λ that cover the range of observed slopes and with μ derived from λ (see the appendix). Conditions above a given curve will lead to droplet

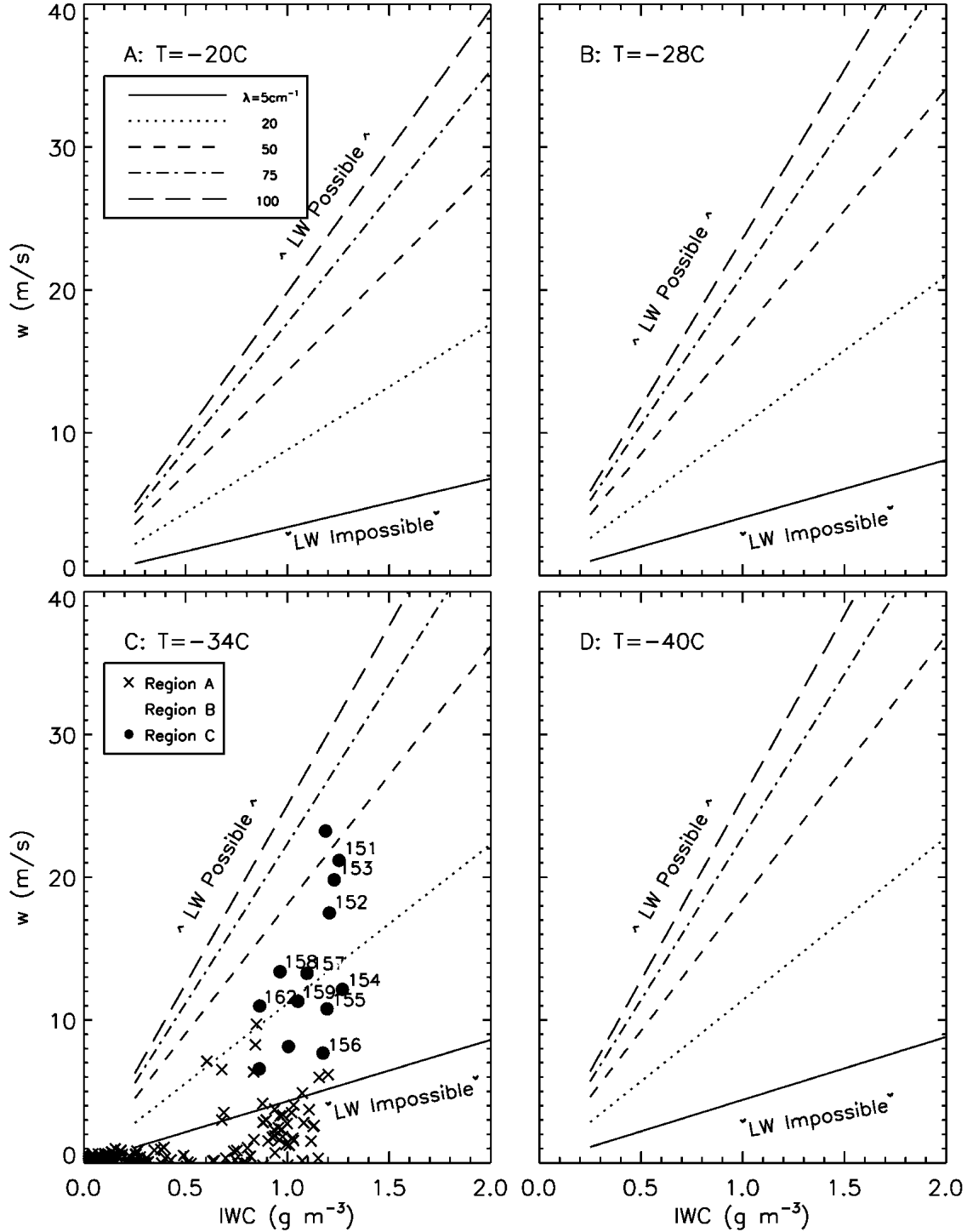


FIG. 15. Curves show the equilibrium vertical velocity (w) needed to balance vapor depletion by a given IWC for the labeled gamma distribution slope (λ), if the RH is 100%. Each panel is a different temperature, and the pressure is taken to be 300 hPa. Data points from the aircraft cloud penetration are shown in (c), as explained in the text.

production and conditions below a curve will not lead to droplet production, assuming that $s = 1.0$. (Homogeneous nucleation is assumed not to occur in this analysis.) Note that with decreasing temperature (panels a-d), the curves shift upward and therefore higher vertical velocities are required to produce LW. This is because the ratio ϕ_3/ϕ_1 increases with decreasing temperature more than the decrease in the ice growth rate with decreasing temperature. Note also that these results are consistent with the findings of Korolev and Mazin (2003), who find that the time scale for quenching supersaturation is determined by the first, not the third moment of the preexisting particle size distribution.

The 1-Hz CVI IWC and w measurements from the aircraft cloud penetration are plotted in Fig. 15c. Interpolated, 1-Hz λ values derived from the 5-s imaging probe size distributions are used to assess those points (with times given in seconds from the beginning of the penetration), where the measured w exceed those needed for LW to be generated if the preexisting ice particles are the only ones that deplete the vapor. Every location in regions B and C could have generated LW, if the preexisting particles $> 100 \mu\text{m}$ were the only ones present. If the gamma distributions were extended downward to 10 rather than $100 \mu\text{m}$ (not shown in the figure), there would be more depletion by the preexisting ice particles. Even so, all but one second in these regions still could have generated LW. With high concentrations of small particles added (through entrainment) to the preexisting population, the RH drops rapidly and LW cannot be produced (see curves in Fig. 13).

The impact of preexisting ice on the droplets observed in the LW region and subsequent homogeneous nucleation is more quantitatively investigated by repeating the model runs in Fig. 13 with the addition of depletion with $\text{IWC}_0 = 0.5 \text{ g m}^{-3}$ and $\lambda = 20 \text{ cm}^{-1}$, $\mu = -1.5$, and size range $0.01\text{--}0.3 \text{ cm}$. Given these approximate updraft-average values, the total preexisting concentration is 0.35 cm^{-3} , which is approximately the concentration of the particles larger than $100 \mu\text{m}$ from Fig. 9. A comparison of Figs. 16 and 13 shows that the concentration of ice particles produced by homogeneous nucleation is minimally affected by the depositional (vapor) growth due to the preexisting ice if $w \geq 10 \text{ m s}^{-1}$. However, if $w = 5 \text{ m s}^{-1}$, the homogeneously nucleated ice concentrations are reduced by about 1/2. Therefore, the concentration of homogeneously produced ice in region C has been appreciably affected by the preexisting large ice lofted from below. Further depletion due to droplet accretion by the preexisting ice is elaborated upon below.

The dependence of the homogeneously produced ice concentration on the diffusional growth of the preexisting ice is shown over a wide range of w and IWC_0 conditions in Fig. 17a for a spectral slope $\lambda = 20 \text{ cm}^{-1}$, where the model was initialized at -20°C using the same CCN distributions as in Fig. 13. In general, the homogeneously nucleated ice concentration decreases

slowly with increasing IWC_0 until a critical threshold is reached where vapor depletion from the preexisting ice exceeds the vapor supply and droplets do not become activated, so the homogeneously nucleated ice concentration decreases rapidly. The preexisting ice has an insignificant effect on the numbers of homogeneously nucleated particles for $w \geq 10 \text{ m s}^{-1}$ and becomes increasingly influential as w decreases from 10 to 1 m s^{-1} . If IWC_0 is about 0.5 g m^{-3} , as observed in the LW region, substantial concentrations of ice will be produced homogeneously if the vertical velocity is greater than about 5 m s^{-1} , and at lower vertical velocities the homogeneous nucleation process is completely suppressed. In an updraft of 20 m s^{-1} even 2 g m^{-3} of large ice is insufficient to affect the homogeneous nucleation process. We therefore again conclude that the absence of LW in region B is due to the small ice presumably entrained into the updraft.

Cloud droplets may be transported through the 0°C level so that they arrive at a temperature of -20°C together with a population of preexisting ice. This LW may act as a source of vapor that offsets the depletion effects of the preexisting ice, with the result that, for $5 \text{ m s}^{-1} < w$, homogeneous nucleation is more likely to occur than was earlier modeled. As a sensitivity study, parcels with $w = 5 \text{ m s}^{-1}$ were initialized at a temperature near -10°C , and the LWC was allowed to build up to about 0.5 g m^{-3} at -20°C before the preexisting ice was allowed to deplete it. The CCN spectrum was modified to give the same droplet concentrations that were found for the runs that started at -20°C . A comparison of the curves labeled 2A and 5A to 2B and 5B in Fig. 17b shows that in weak updrafts, preexisting LW makes the homogeneous nucleation process more likely to occur.

The threshold (IWC_0, w) conditions necessary to produce LW based on the calculations from Fig. 17 are summarized in Fig. 18. Homogeneous nucleation is predicted to occur for vertical velocities above each curve and is suppressed below each curve by the given IWC_0 . The thin shaded region below the upper curve (and each curve but only the upper curve is shaded for clarity) indicates conditions where “regular” homogeneous nucleation will not occur near the -35°C level because the preexisting ice has limited the maximum RH to below 100% and prevented droplet activation, but homogeneous nucleation of these small solution droplets will eventually occur at a lower temperature when the homogeneous nucleation rate increases sufficiently by continued uplift. In other words, homogeneous nucleation can occur at any temperature level in an updraft, but only for a narrow range of conditions, outside of which homogeneous nucleation is either suppressed completely or occurs near -35°C . Delayed homogeneous nucleation results in far lower ice concentrations ($< 1 \text{ cm}^{-3}$) because the first solution droplets to freeze will further reduce the RH by increasing the vapor depletion and suppress further homogeneous nucleation.

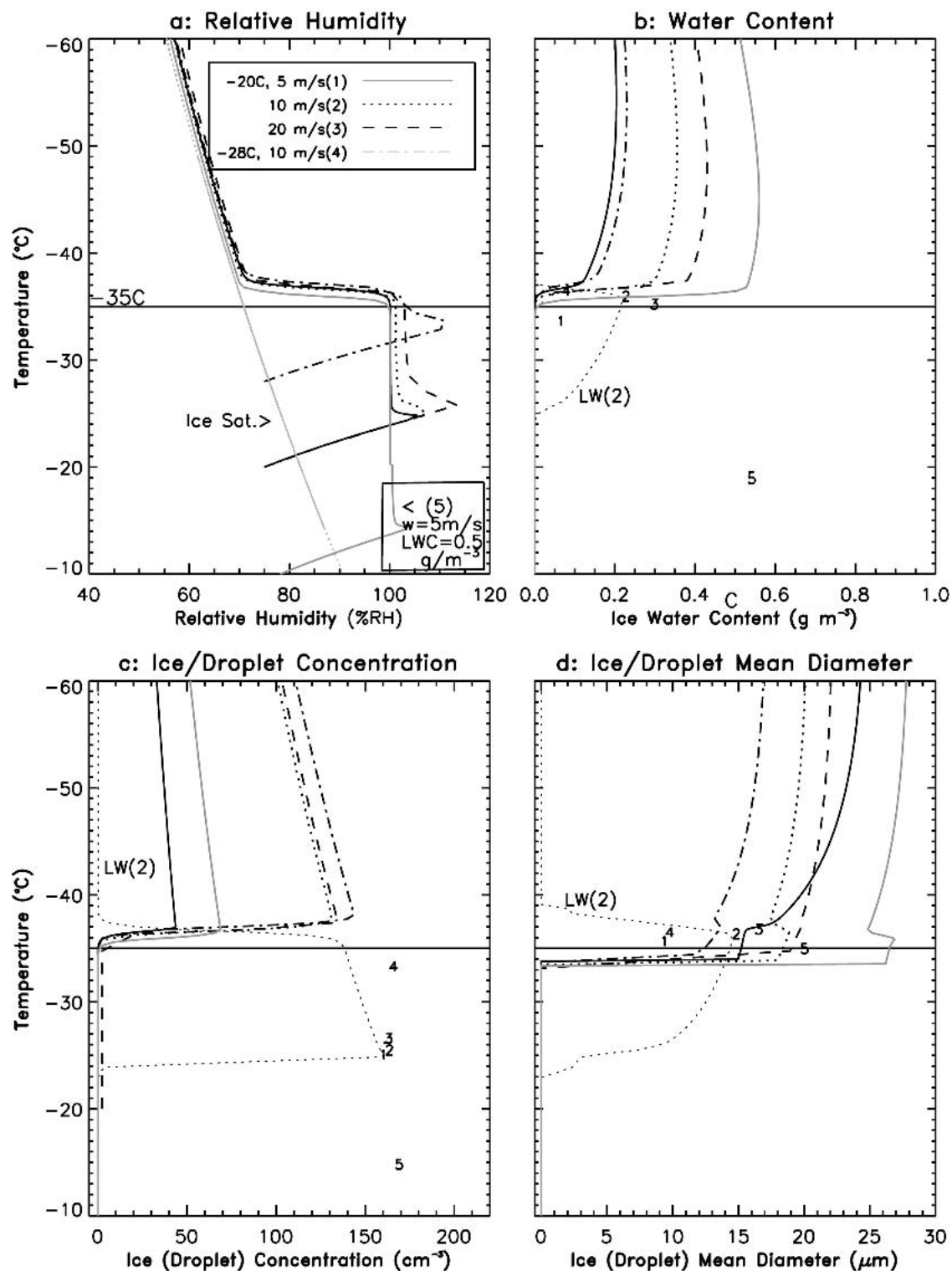


FIG. 16. As for the model calculations shown in Fig. 13 except additional vapor depletion from a preexisting IWC of 0.5 g m^{-3} is included. The preexisting IWC is specified by a gamma size distribution with spectral slope $\lambda = 20 \text{ cm}^{-1}$, dispersion $\mu = -1.5$, and maximum particle size 0.3 cm . The total concentration of pre-existing ice is 0.35 cm^{-3} .

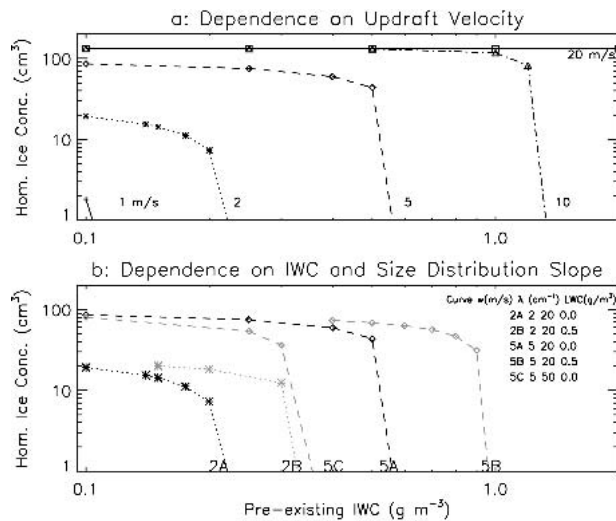


FIG. 17. Ice concentrations formed in the updrafts from the homogeneous nucleation model, with calculations beginning at the -20°C level. (a) Concentrations with varying w , $\lambda = 20\text{ cm}^{-1}$, $\text{LWC} = 0\text{ g m}^{-3}$ transported to the -20°C level. (b) Concentrations produced for 2 and 5 m s^{-1} updraft velocities, with $\text{LWC} = 0$ and 0.5 g m^{-3} at the -20°C level, and for two values of λ .

b. Droplets transported from below

We now address the question of whether it is more likely for cloud droplets to be transported from cloud base or through midlevel entrainment to the homogeneous nucleation layer. Cloud droplets, lofted in updrafts from cloud base or produced by entrainment toward the -35°C level, will be depleted either partially or entirely by the preexisting ice. To examine the fate of the cloud droplets under such conditions that could not be readily considered in the homogeneous nucleation model, graupel growth and droplet collection was examined using the 1D graupel growth model of Heymsfield (1982). The size distributions were taken to be the gamma distributions initialized earlier. The methods used to treat the graupel growth and droplet collection are discussed in the appendix.

Figure 19 shows the ratio of the LWC to its initial value (LWC_0) as a function of temperature in the updraft for model runs that begin at a temperature of -20°C . The runs are for $\lambda = 20\text{ cm}^{-1}$ and $\lambda = 100\text{ cm}^{-1}$ (right columns), with IWC_0 and vertical velocities increasing from the upper to the lower panels. Monodisperse cloud droplet size distributions of diameters ranging from 3 to $20\text{ }\mu\text{m}$ are used to show the effects of droplet size on the ice particle–droplet collection efficiencies (E). The sources used to derive E are given in the appendix. Typical values of E for 0.05-cm diameter graupel range from 0 for droplets of diameter $<4\text{ }\mu\text{m}$, to 0.61 at $10\text{ }\mu\text{m}$, and to 0.86 at $20\text{ }\mu\text{m}$. For 0.2-cm graupel, E becomes 0 for droplets $<5\text{-}\mu\text{m}$ diameter, 0.48 for $10\text{-}\mu\text{m}$ diameter droplets, and 0.81 for $20\text{-}\mu\text{m}$ droplets. Monodisperse size distributions have the

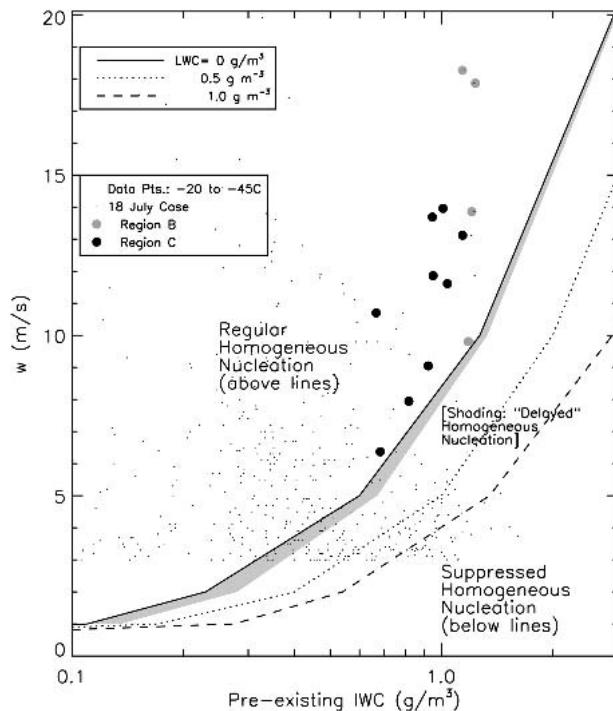


FIG. 18. Model calculations, as in Fig. 17, of the threshold conditions separating the conditions where homogeneous nucleation occurs and where it is suppressed, as defined by production of ice in concentrations exceeding 1 cm^{-3} . Homogeneous nucleation will occur if the vertical velocity is above the curve for a given preexisting IWC. Curves show the effect of the specified LWC at the -30°C level. The slope of the size distribution is 20 cm^{-1} . The shaded region for “delayed” homogeneous nucleation is discussed in the text.

added benefit that the ratio LWC/LWC_0 is equivalent to the ratio of the droplet concentration to the initial value. Runs for $E = 1$ are also shown. Droplets are more likely to be lofted to the -35°C level with increasing vertical velocity (less time for droplet collection), decreasing IWC (fewer ice collectors) and decreasing λ (smaller total population in cross-sectional area). Most notably, collection efficiency effects have a profound influence on the depletion process, with small cloud droplets being minimally reduced through collection. We suggest that this is why the small cloud droplets that were observed in region C, presumably the result of entrainment and droplet activation, were transported to the -35°C region in the updraft whereas potentially larger droplets in the updraft core were nonexistent.

c. Preexisting ice observed in subtropical and tropical convection

Given the sensitivity of the homogeneous nucleation process in convective updrafts to the preexisting ice, typical values of IWC measured in convective updrafts ($w \geq 3\text{ m s}^{-1}$) are investigated as a function of w and T in Fig. 20 using data from four field experiments. During CRYSTAL–FACE, such updrafts were sampled on

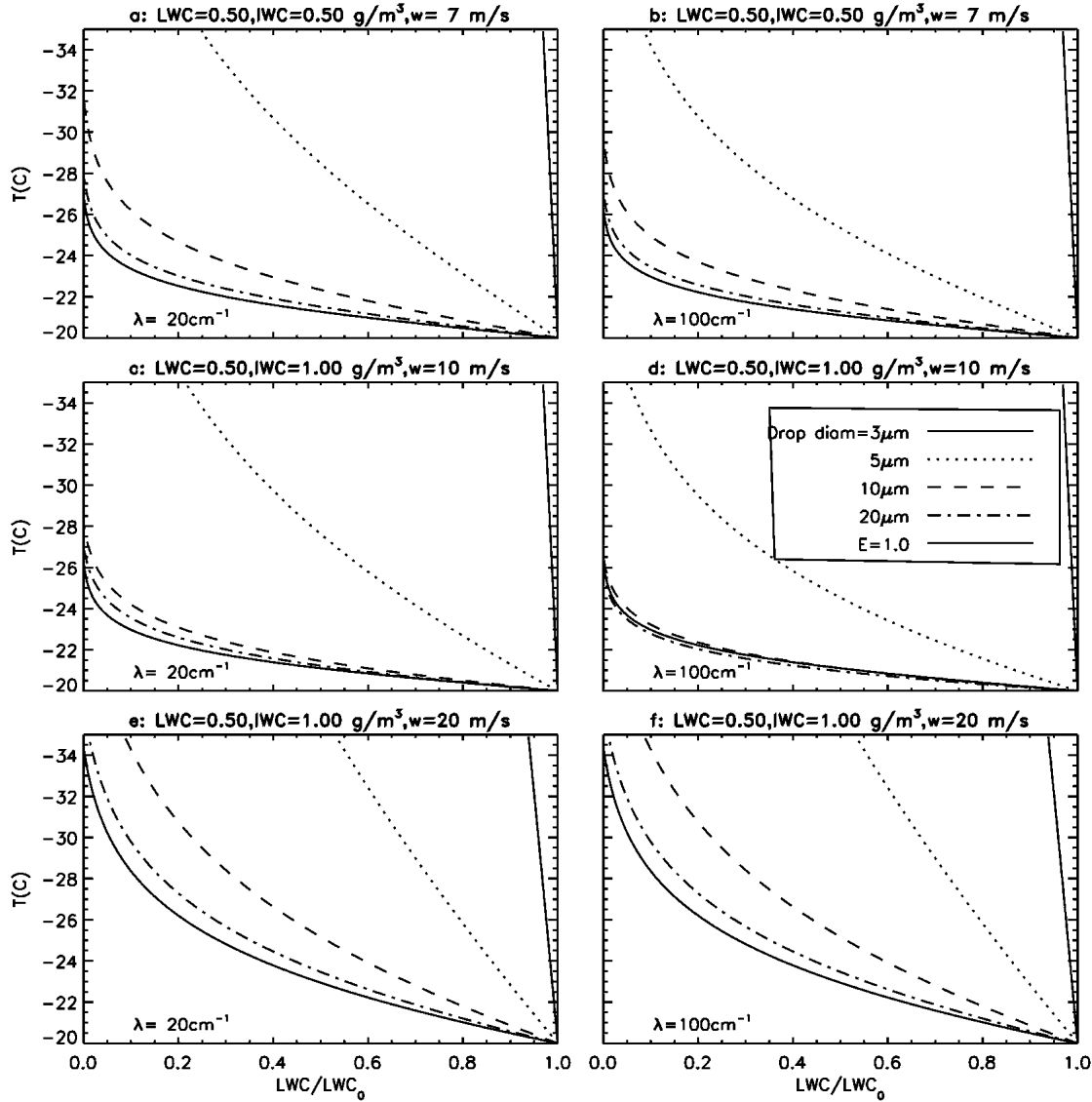


FIG. 19. Depletion of liquid water content by population of ice particles, using a 1D parcel model with prescribed w , LWC, and IWC for calculations that begin at a temperature of -20°C . Monodisperse cloud droplet populations for different cloud droplets size are used to derive the droplet-ice particle collection efficiencies, as well as assuming the collection efficiency is unity. PSD slope is (left) $\lambda = 20 \text{ cm}^{-1}$; (right) $\lambda = 100 \text{ cm}^{-1}$.

18, 25, and 28 July. During the Tropical Rain Measuring Mission (TRMM) experiment at Kwajalein, Marshall Islands (KWAJEX), the Citation sampled updrafts on 30 August and 5 September 1999. During the Convection and Moisture Experiment (CAMEX-4) and the Keys Area Microphysics Project (KAMP) in 2001, the NASA DC-8 aircraft penetrated such updrafts off the coast of Florida on nine days.

The frequency of occurrence of IWC measurements below a threshold value (Fig. 20a) indicates that the IWC tends to increase with increasing vertical velocity. Considering the log scale, the vast majority of the measured IWC values are in the range $0.1\text{--}0.5 \text{ g m}^{-3}$. Note that only one point exceeded 1 g m^{-3} .

The IWC decreases by about an order of magnitude over the temperature range from -20° to -60°C (Fig. 20b). In the critical temperature range from -25° to -34°C for evaluating the effect of preexisting ice on the homogeneous nucleation process, the mean IWC is $0.42 \pm 0.30 \text{ g m}^{-3}$ and only 12% of the values exceed 0.5 g m^{-3} , indicating that the model calculations used in this section are relevant to tropical convective updrafts studied in earlier experiments. The gamma PSD slope (λ , Fig. 20c) has a broad range ($5\text{--}200 \text{ cm}^{-1}$), and little dependence on T . The mean value, $\bar{\lambda} = 59 (\pm 37) \text{ cm}^{-1}$, is somewhat higher than the mean value of 20 cm^{-1} for the 18 July cloud penetration. Removing the large grouping of points with $\lambda \approx 100 \text{ cm}^{-1}$, which signifies a

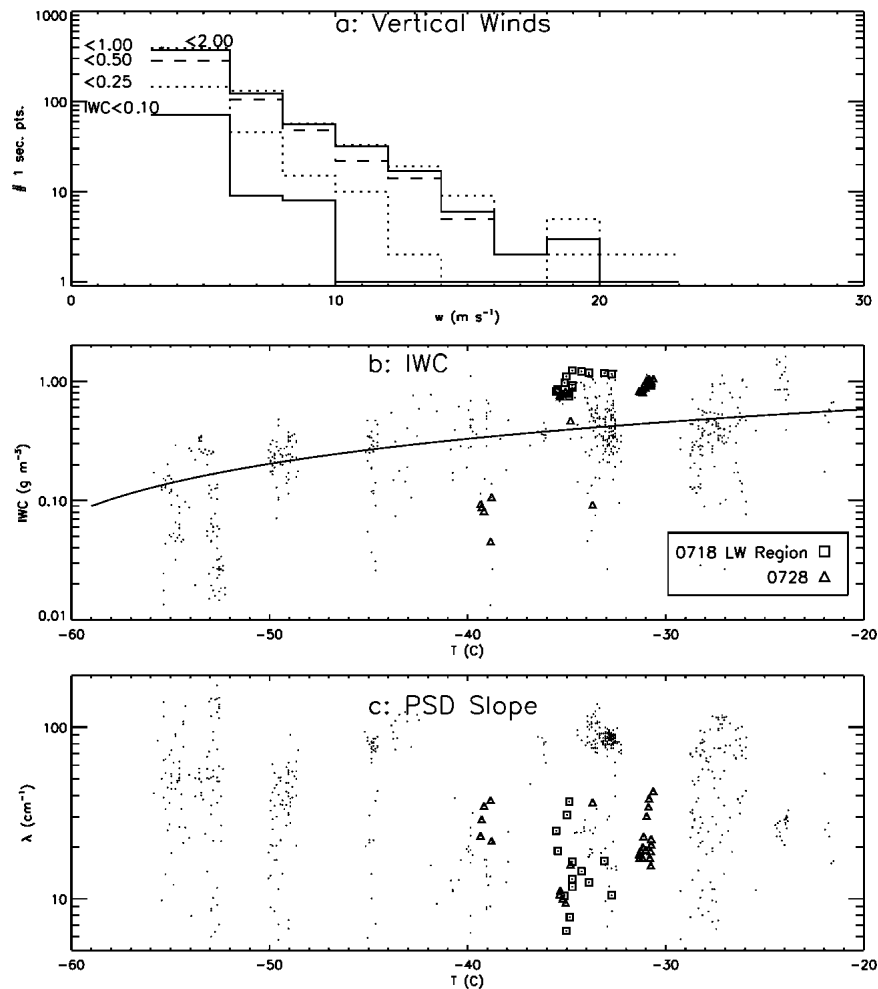


FIG. 20. Imaging probe measurements of IWC from several field programs as a function of vertical velocity (w) and temperature (T), for all instances where $w > 3 \text{ m s}^{-1}$ from a number of field programs. (a) Frequency distributions of instances when the IWC was below the labeled values, as a function of w . (b) IWC as a function of T , with squares indicating the cloud penetration in this study, and triangles indicating the 28 Jul CRYSTAL-FACE case. A solid line indicates a linear curve fitted through the data. (c) Spectral slope of the size distributions as a function of T .

dominance of small particles and possible homogeneous freezing or ice particle entrainment, λ falls in the range from about 20 to 50 cm^{-1} .

The data points plotted in Fig. 18 show the w -IWC observations from the various tropical convective cloud penetrations between -20° and -45°C . Diffusional ice growth limits homogeneous nucleation in tropical convective clouds with vertical velocities above 4 m s^{-1} and it is increasingly unlikely below this.

7. Summary and conclusions

This study has examined the role of the homogeneous ice nucleation process in a tropical convective environment. The primary observational data were obtained during an aircraft penetration of a vigorous con-

vective cloud and associated anvil at a temperature of about -35°C . Parcel (1D) models of droplet and ice crystal growth and homogeneous nucleation were used to understand the observations and to evaluate the influence of homogeneous nucleation on the microphysical and radiative properties of tropical convective anvils.

The analysis suggests that homogeneous ice nucleation occurs in tropical convective updrafts at temperatures between -35.5° and -37.5°C when the vertical velocity exceeds $5\text{--}10 \text{ m s}^{-1}$. In updrafts of that magnitude, ice particles that form through nonhomogeneous processes at higher temperatures may be unable to deplete the water vapor and prevent droplet activation and subsequent homogeneous nucleation. Furthermore, it is found that most large droplets and drops originating in the lower levels of a cloud are likely to be

collected by large ice particles before they reach the homogeneous nucleation level. It is shown that midtropospheric aerosols entrained into the updrafts are the likely source of small ($<20 \mu\text{m}$) droplets that persist in the updraft to the homogeneous nucleation level, in part due to the low collection efficiency of small droplets by large ice particles.

This study suggests that the role of the homogeneous nucleation process may change with time through the life cycle of a convective cloud and is strongly influenced by the environmental airflow. In the competition between vapor supplied by cooling in the updraft and vapor depleted by growth of the droplet and ice population, together with droplet collection through accretion, homogeneous nucleation can be suppressed if either the updraft speed is below some threshold or the integrated vapor depletion exceeds some threshold. For strong convection (e.g., updrafts $> 5\text{--}10 \text{ m s}^{-1}$), it is shown that low concentration of large, heterogeneously produced ice particles are not sufficient to prevent droplet activation and subsequent homogeneous nucleation, but high concentrations of small ice particles typically produced by homogeneous nucleation are sufficient to deplete the water vapor and suppress further nucleation, even in very strong updrafts. Downward transport and mixing of air laden with homogeneously nucleated ice particles back into the updraft below the homogeneous nucleation level can completely suppress further homogeneous nucleation, as occurred for this case study in the downwind portion of the updraft core. In contrast, nucleation in the upwind portion of the updraft core in this case study continued beyond the early portion of the cloud lifetime because ice particles were carried downwind and were not available for downward transport and entrainment back into the updraft.

The size-dependent microphysical observations indicate that the small particles dominate the radiative properties and ice water content in the sampled updraft. These particles are transported in the strong updrafts into the anvil. The anvil is therefore composed of large particles that were produced heterogeneously (but have relatively little radiative impact) and small particles that were produced homogeneously (with a large radiative impact). Once in the anvil, aggregation will reduce the radiative and ice water content contributions by the small particles (Heymsfield et al. 2002).

This study has raised several important questions:

- What is the rate of collection and removal of small homogeneously nucleated ice particles by the larger heterogeneously nucleated ice within the anvil, and what is the rate of sublimation of the small ice? The decrease in the contribution of small ice particles with increasing distance downwind from the convective core (Fig. 5) suggests that these rates appreciably affect the concentrations of small particles, with implications for anvil radiative properties.
- What are the relative roles of large droplets and

drops that originated at cloud base versus those originating at midlevels on the homogeneous freezing process?

- What is the temperature distribution of raindrop freezing in the updrafts?
- To what extent does the abrupt, homogeneous freezing of droplets strengthen the updraft?

Direct, in situ measurements of the influence of the heterogeneously nucleated ice on the homogeneous nucleation process and the effects of entrained aerosol and ice particles on updraft microphysics and the homogeneous nucleation process are needed. Three-dimensional cloud models with detailed microphysics are needed to provide a detailed analysis of the effects of entrainment and turbulence on the homogeneous nucleation process. The results from this study can also be evaluated from such measurements and models.

Acknowledgments. The authors are indebted to the crew of the University of North Dakota Citation aircraft for their help with the data collection, and to Nancy Knight for her review of this manuscript. This research was supported by the NASA Crystal Program, Don Anderson, and Hal Maring, program managers.

APPENDIX

Calculation of the Diffusional Growth Rate of an Ice Particle Population

The time rate of change of ice mass depletion by a population of quasi-spherical ice particles (graupel, aggregates, etc.) as in Fig. 6, assuming a relatively constant pressure, is

$$\frac{d(IWC_0)}{dt} = 4\pi G' \int_0^\infty N(D)C(D)S_i F dD$$

$$= 2\pi G' S_i N_0 \bar{F} \int_0^\infty D^{(1+\mu)} e^{-\lambda D} dD, \quad (A1)$$

$$= 2\pi G' S_i \bar{F} \frac{\Gamma(2+\mu)}{\lambda^{(2+\mu)}}, \quad (A2)$$

where G' is a temperature and pressure dependent term, N is the concentration, which on the right side of Eq. (1) is written as a gamma distribution,

$$N(D) = N_0 D^\mu e^{-\lambda D}, \quad (A3)$$

with N_0 as the intercept parameter, μ the dispersion, and λ the slope of the PSD, $C \approx D/2$ is the shape factor, F is the ventilation coefficient, and \bar{F} the mean for the PSD, and S_i is the ice supersaturation. Using the analytic expression for the IWC for a gamma distribution,

$$IWC_0 = \frac{\pi}{6} \bar{\rho}_e N_0 \frac{\Gamma(4+\mu)}{\lambda^{(4+\mu)}},$$

then

$$\frac{dIWC_0}{dt} = 12G' \bar{F} S_i \frac{IWC_0^2}{(3+\mu)(2+\mu)} \quad (A4)$$

as has been found by others.

Gamma distributions were fitted to the ice PSDs. The three unknown coefficients in Eq. (A1) were reduced to two by fitting a relationship between λ and μ from size distributions in updrafts. Because few samples were obtained for the 18 July case, several hundred size distributions obtained for updrafts $> 3 \text{ m s}^{-1}$ (described in section 6) were factored into the dataset and then a curve was fitted to the data:

$$\mu = 0.016\lambda^{1.1} - 2.0. \quad (\text{A5})$$

In our wave cloud model, the concentrations of large ice particles were found in 15 equally spaced size bins from 200 to 3000 μm using the following approach. The IWC can be represented analytically by

$$\text{IWC} \approx \frac{\pi}{6} \bar{\rho}_e N_0 \frac{\Gamma(4 + \mu)}{\lambda^{(4 + \mu)}}, \quad (\text{A6})$$

Average values of $\lambda = 20 \text{ cm}^{-1}$ and μ given by Eq. (A5) are taken to represent the PSDs in the updraft core. A mean effective ice density $\bar{\rho}_e$ of 0.15 g m^{-3} is taken for the large ice for the updraft region based on data from this case in Heymsfield et al. (2004). For a given IWC value, N_0 and N in each of the 15 size bins can therefore be readily obtained. Ventilation coefficients were chosen based on spherical particles in Heymsfield (1982) and the terminal velocities given in Mitchell and Heymsfield (2005) for graupel.

The growth of graupel and the depletion of water vapor in updrafts were derived using the graupel model described in Heymsfield (1982). An initial graupel size distribution is specified as described above but in 100 size bins, and new size distribution is calculated for each 15 m in the vertical. The time required for graupel of each size to be lifted through this height increment is derived from the difference between the air and particle terminal velocity. Over this period, growth is calculated assuming an accretional density of 0.15 g m^{-3} , the new particle size and terminal velocity is calculated, and the concentration is adjusted to reflect the change in the terminal velocity. This procedure is done for all particles in the size distribution. The liquid water is depleted in the process, with collection efficiencies based on those for rigid spheres by Beard and Grover (1974), as described in Heymsfield (1982).

REFERENCES

- Beard, K. V., and S. N. Grover, 1974: Numerical collision efficiencies for small raindrops colliding with micron size particles. *J. Atmos. Sci.*, **31**, 543–550.
- Field, P. R., R. Wood, P. R. A. Brown, P. H. Kaye, E. Hirst, R. Greenaway, and J. A. Smith, 2003: Ice particle interarrival times measured with a fast FSSP. *J. Atmos. Oceanic Technol.*, **20**, 249–261.
- Fridlind, A. M., and Coauthors, 2004: Evidence for the predominance of mid-tropospheric aerosols as subtropical anvil nuclei. *Science*, in press.
- Gerber, H., V. Takano, T. J. Garrett, and P. V. Hobbs, 2000: Nephelometer measurements of the asymmetry parameter, volume extinction coefficient, and backscatter ratio in Arctic clouds. *J. Atmos. Sci.*, **57**, 3021–3034.
- Hess, S. L., 1959: *Introduction to Theoretical Meteorology*. H. Holt and Co., 362 pp.
- Heymsfield, A. J., 1973: Cirrus uncinus generating cells. Chapter 5: Ice nucleation and growth of cirrus particles. Ph.D. dissertation, University of Chicago, 269 pp.
- , 1975: Cirrus uncinus generating cells and the evolution of cirriform clouds. Part III: Numerical computations of the growth of the ice phase. *J. Atmos. Sci.*, **32**, 820–830.
- , 1982: A comparative study of the rates of development of potential graupel and hail embryos in High Plains storms. *J. Atmos. Sci.*, **39**, 2867–2897.
- , and M. Sabin, 1989: Cirrus crystal nucleation by homogeneous freezing of solution droplets. *J. Atmos. Sci.*, **46**, 2252–2264.
- , and L. M. Miloshevich, 1993: Homogeneous ice nucleation and supercooled liquid water in orographic wave clouds. *J. Atmos. Sci.*, **50**, 2335–2353.
- , P. N. Johnson, and J. E. Dye, 1978: Observations of moist adiabatic ascent in northeast Colorado cumulus congestus clouds. *J. Atmos. Sci.*, **35**, 1689–1703.
- , J. E. Dye, and C. J. Biter, 1979: Overestimates of entrainment from wetting of aircraft temperature sensors in cloud. *J. Appl. Meteor.*, **18**, 92–95.
- , A. Bansemer, P. R. Field, S. L. Durden, J. Stith, J. E. Dye, W. Hall, and T. Grainger, 2002: Observations and parameterizations of particle size distributions in deep tropical cirrus and stratiform precipitating clouds: Results from in situ observations in TRMM field campaigns. *J. Atmos. Sci.*, **59**, 3457–3491.
- , C. G. Schmitt, C. Twohy, and M. R. Poellet, 2004: Effective ice particle densities derived from aircraft data. *J. Atmos. Sci.*, **61**, 982–1003.
- Khelif, D., S. P. Burns, and C. A. Friehe, 1999: Improved wind measurements on research aircraft. *J. Atmos. Oceanic Technol.*, **16**, 860–875.
- Koop, T., B. Luo, A. Tsias, and T. Peter, 2000: Water activity as the determinant for homogeneous ice nucleation in aqueous solutions. *Nature*, **406**, 611–614.
- Korolev, A. V., and I. P. Mazin, 2003: Supersaturation of water vapor in clouds. *J. Atmos. Sci.*, **60**, 2957–2974.
- Krämer, B., O. Hübner, H. Vortisch, L. Wöste, T. Leisner, M. Schwell, E. Rühl, and H. Baumgärtel, 1999: Homogeneous nucleation rates of supercooled water measured in single levitated microdroplets. *J. Chem. Phys.*, **111**, 6521–6527.
- Lawson, R. P., L. J. Angus, and A. J. Heymsfield, 1998: Cloud particle measurements in thunderstorm anvils and possible weather threat to aviation. *J. Aircr.*, **35**, 113–121.
- May, R. D., 1998: Open-path, near-infrared tunable diode laser spectrometer for atmospheric measurements of H_2O . *J. Geophys. Res.*, **103**, 19 161–19 172.
- Mazin, I. P., A. V. Korolev, G. A. Isaac, and A. J. Heymsfield, 2001: Thermodynamics of icing cylinder for measurements of liquid water content in supercooled clouds. *J. Atmos. Oceanic Technol.*, **18**, 543–558.
- Mitchell, D. L., and A. J. Heymsfield, 2005: Refinements in the treatment of ice particle terminal velocities: Highlighting aggregates. *J. Atmos. Sci.*, in press.
- Ogren, J. A., J. Heintzenberg, and R. J. Charlson, 1985: In-situ sampling of clouds with a droplet to aerosol converter. *Geophys. Res. Lett.*, **12**, 121–124.
- Paluch, I. R., 1979: The entrainment mechanism in Colorado cumuli. *J. Atmos. Sci.*, **36**, 2467–2478.
- Rosenfeld, D., and W. L. Woodley, 2000: Deep convective clouds with sustained supercooled liquid water down to -37.5°C . *Nature*, **405**, 440–442.
- Sassen, K., and G. C. Dodd, 1988: Homogeneous nucleation rate for highly supercooled cirrus cloud droplets. *J. Atmos. Sci.*, **45**, 1357–1369.
- Twohy, C. H., A. J. Schanot, and W. A. Cooper, 1997: Measurement of condensed water content in liquid and ice clouds using an airborne counterflow virtual impactor. *J. Atmos. Oceanic Technol.*, **14**, 197–202.